



TECHNISCHE
UNIVERSITÄT
WIEN

Vienna University of Technology

DIPLOMARBEIT

Comparison of Different Attenuation Correction Methods in Hybrid PET/MR Brain Imaging

Ausgeführt am

Institut für Angewandte Physik¹

der Technischen Universität Wien

in Zusammenarbeit mit der

Universitätsklinik für Psychiatrie und Psychotherapie²

der Medizinischen Universität Wien

unter der Anleitung von

Ao. Univ. Prof. Dr. Martin Gröschl¹

Assoc. Prof. Dr. Rupert Lanzenberger, PD²

Ass. Prof. Dr. Andreas Hahn²

durch

Lucas Rischka

Währinger Straße 100/18

1180 Wien

Datum

Unterschrift (Student)

Acknowledgements

I want to express my gratitude to my supervisor at the Vienna UT Prof. Martin Gröschl who offered me the opportunity to write my diploma thesis at the Institute of Applied Physics. I also want to thank Prof. Rupert Lanzenberger from the Medical University of Vienna for making me a part of his research group “Neuroimaging Labs” and the unique chance to write my diploma thesis in the field of PET/MR. Furthermore, I want to express my gratitude to my mentor and co-supervisor Ass. Prof. Andreas Hahn for his tremendous and untiring support, the inspiring discussions and his motivational words which helped me to get through these intensive times of writing this diploma thesis. Finally, I want to thank my mother, my stepfather and my grandfather for their encouragement, patience and financial support.

Science is a way of life. Science is a perspective. Science is the process that takes us from confusion to understanding in a manner that's precise, predictive and reliable - a transformation, for those lucky enough to experience it, that is empowering and emotional.

- **Brian Greene, Physicist**

Abstract

The development of hybrid positron emission tomography/magnetic resonance imaging (PET/MR) systems opened the opportunity for a simultaneous acquisition of PET emission data and (functional) MR imaging. However, an unresolved issue is the correction of attenuated photons. The main contributor to attenuation is bone due to its chemical and physical properties. However, it is not possible to fully depict this tissue with MRI because of its low abundance of hydrogen atoms. An appropriate attenuation correction (AC) is essential for correct quantification in research studies but also for the clinical routine, e.g. tumor classification. In research studies a common way to overcome the issue with AC in PET/MR is the acquisition of a low-dose computed tomography scan (CT) and its application to the PET emission data as AC map. However, the separate recording of a CT is inconvenient. It leads to an additional radiation exposure to the patients, a logistical issue since the patients have to be transferred to a different scanner and also to a technical challenge because the CT has to be preprocessed before it can be applied. Therefore, alternative approaches with less effort and correct AC are highly desirable.

In this work, four different AC approaches were compared to the gold-standard AC CT, namely two MRI-segmentation based approaches which were provided by the vendor (DIXON, UTE), one atlas-based approach based on a database with MRI-CT pairs (pseudoCT) and lastly, a transmission scan generated by rotating radioactive rod sources from a PET-only system (TX). The differences were compared on a region-of-interest but also on a voxel-wise basis.

The results revealed a great performance variation for all attenuation correction approaches. The atlas-based approach (pseudoCT) performed best in terms of reproducibility and bias whereas the other approaches showed great underestimation of the uptake values across the whole brain. The segmentation based approaches displayed a greater miscalculation of the uptake in the proximity to the skull whereas the highest error for the TX was found close to the center of the brain. The observed results were in accordance with previous works.

Based on the findings the atlas-based approach seems to be a promising substitution for the CT even though it shows slight fluctuations in the occipital and frontal region. However, in its current form the pseudoCT might only be applicable on research studies where time is a minor issue. Differently, in clinical routine a drawback of this approach is the necessity of preprocessing of the pseudoCT which is unfeasible for clinics.

Kurzfassung

Die Einführung der hybriden Positronenemissionstomographie/Magnetresonanztomographie (PET/MR) Systeme eröffnete die Möglichkeit der simultanen Aufnahme von PET-Daten und (funktionellen) MR Bildern. Ein bisher ungelöstes Problem ist allerdings die Schwächungskorrektur der Photonen. Der überwiegende Anteil an Schwächung ist aufgrund seiner chemischen und physikalischen Eigenschaften Knochen zuzuordnen. Wegen seines niedrigen Gehalts an Wasserstoffatomen ist es nicht möglich Knochengewebe vollständig im MR abzubilden. Eine korrekte Schwächungskorrektur ist allerdings essentiell um die Daten einerseits in Forschungsstudien korrekt quantifizieren zu können und andererseits, für die Klinik, um beispielsweise Tumor richtig zu klassifizieren. In Forschungsstudien wird das Problem der Schwächungskorrektur meist mit der Aufnahme eines niedrig dosierten Bildes in einem Computertomographen (CT) und dessen Anwendung auf die PET-Daten umgangen. Dieses zusätzlich aufgenommene CT ist allerdings unpraktisch. Es bedeutet eine zusätzliche Strahlenexposition für den Patienten, ist eine logistische Herausforderung und bringt weitere technische Probleme. Aus diesem Grund sind korrekte und gleichzeitig einfach zu implementierende Alternativlösungen eine essentielle Anforderung an hybride PET/MR Systeme.

In dieser Arbeit wurden vier verschiedenen Ansätze der Schwächungskorrektur mit dem Goldstandard CT verglichen, nämlich zwei Arten die auf der Segmentierung von MR Bildern basieren und vom Hersteller des Geräts zur Verfügung gestellt werden (DIXON, UTE), ein Ansatz der auf einer Datenbank, gefüllt mit MR-CT Paaren basiert (pseudoCT) und zuletzt, eine Transmissionsmessung die durch rotierende, radioaktive Stabquellen zustande kommt, welche auf einem gewöhnlichen PET aufgenommen wurde. Die Unterschiede wurden auf Basis von Regionen als auch Voxel (volumetrische Pixel) überprüft.

Die Resultate zeigten eine große Variation zwischen den unterschiedlichen Schwächungskorrekturansätzen. Der Ansatz, der auf MR-CT Paaren basiert, schnitt im Sinne von Reproduzierbarkeit und Fehler am besten ab während die anderen Arten eine große Unterschätzung der Aktivität im gesamten Hirn zeigten. Die Ansätze die auf Segmentierung basierten zeigten eine größere Fehlberechnung der Aktivität in der Nähe des Schädelknochen, bei der Schwächungskorrektur mittels Transmissionscan war der Fehler im Bereich des Zentrums des Hirns am größten. Die gefunden Resultate stimmten mit früher publizierten Ergebnissen überein.

Basierend auf den Resultaten scheint der datenbankbasierte Ansatz ein vielversprechender Ersatz für das CT zu sein, auch wenn er leichte Unsicherheiten im frontalen und okzipitalen Bereich zeigt. Das pseudoCT könnte derzeit nur in Forschungsstudien angewandt werden, wo Zeit eine geringere Rolle spielt. Der Nachteil des Ansatzes ist nämlich die Notwendigkeit dessen Prozessierung bevor er angewandt werden kann. Diese Prozessierung ist derzeit in der Klinik nicht möglich.

Table of contents

1.	Motivation and aim of the work	7
2.	Physical Background	8
2.1.	Positron Emission Tomography	8
2.1.1.	Nuclear Physics	8
2.1.2.	Radiotracer	9
2.1.3.	Data acquisition	10
2.1.4.	Image reconstruction	11
2.2.	Hybrid PET/CT scanners.....	16
2.3.	Hybrid PET/MR scanners.....	17
2.3.1.	MRI	17
2.3.2.	Challenges	17
2.3.3.	Assets.....	18
3.	Methods	20
3.1.	Population.....	20
3.2.	Measurement	20
3.3.	Attenuation correction.....	21
3.3.1.	Attenuation correction with CT.....	21
3.3.2.	Attenuation correction with pseudoCT.....	25
3.3.3.	Attenuation correction with segmentation approaches.....	25
3.3.3.1.	Attenuation correction with DIXON	26
3.3.3.2.	Attenuation correction with UTE	27
3.3.4.	Attenuation correction with transmission scan.....	28
3.4.	Image reconstruction	29
3.5.	Image preprocessing.....	30
3.6.	Image postprocessing and statistics.....	32
4.	Results	34
4.1.	Attenuation correction with pseudoCT	34
4.2.	Segmentation	35
4.2.1.	Attenuation correction with DIXON.....	35
4.2.2.	Attenuation correction with UTE	40
4.3.	Attenuation correction with transmission.....	42
5.	Discussion	48
6.	Conclusion.....	58

7. References	59
Table of figures	63

1. Motivation and aim of the work

Multimodal imaging receives growing attention in research and also in clinical routine. With the introduction of hybrid systems, combining positron emission tomography and magnetic resonance imaging (PET/MR), it was possible to use both modalities simultaneously having perfectly aligned images. For brain research this means for example, measuring changes in brain activity with functional MRI, at the same time as molecular information (e.g. metabolism, receptors).

A drawback of PET/MRI is the absence of adequate bone depiction in MRI images because of the low abundance of hydrogen atoms. Since bone is primarily responsible for photon attenuation it is difficult to realize correct attenuation correction (AC) of PET images obtained from hybrid PET/MR systems. This issue is not present in stand-alone PET or hybrid PET/CT systems, since AC is realized by an external radiation source or the CT, respectively. Accurate AC is however an essential prerequisite for correct quantification of tracer uptake in clinical routine for diagnosis and therapy as well as in research applications. Therefore, MRI data has to be further processed to be used for correct quantification.

The aim of this retrospective work was an evaluation of different AC methods compared to the gold standard computed tomography (CT) scan on a region-of-interest and voxel-wise basis. The results should reveal an AC solution which performs as good as the low-dose CT in terms of reproducibility and bias in order to obviate the need for a separately acquired CT scan. Hence, radiation exposure to the patient could be reduced and registration processes between CT and PET are circumvented. In addition to the quantitative evaluation, ease of implementation for each of the approaches will be discussed, which is an important aspect for the application in clinical routine.

For this purpose four different AC maps were compared to the gold standard CT, namely two MRI-segmentation based approaches which were provided by the vendor (DIXON, UTE), one atlas-based approach based on a database with MRI-CT pairs (pseudoCT) and lastly, a transmission scan generated by rotating rod sources from a PET-only system (TX).

2. Physical Background

The following chapter introduces the reader to the physical background of the used modalities to make the main chapters of this work comprehensible.

The information of this chapter is derived from Bailey et al. (2004), Phelps et al. (2006) or Saha (2005) if not stated differently.

2.1. Positron Emission Tomography

Positron emission tomography (PET) revolutionized nuclear medicine and was invented by David E. Kuhl, Luke Chapman and Roy Edwards in the late 1950s. PET detects radioactive decays of positron emitting isotopes and together with the incorporated biological tracer substance it is a modality to depict the molecular information of an examined area.

2.1.1. Nuclear Physics

The principle of PET is the decay of radioactive atoms and a process called annihilation. Radioactive atoms undergo spontaneous radioactive decay with a certain rate defined as the half-life. The half-life is defined as the time when 50% of a present amount of instable nuclei decayed. The curve of the decay is exponential and therefore, the amount of radioactive atoms after a time t has passed can be calculated with an exponential function:

eq. 1
$$A_t = A_o * e^{(-\lambda t)}$$

A_tactivity at time point t	A_oactivity at time point 0
λdecay constant	t ... time point

The activity is given as disintegrations per second (DPS) in the SI unit Becquerel ([Bq]) with 1 Bq equal to 1 DPS.

There are several types of how instable nuclei can decay namely alpha (α), beta (β) and gamma (γ) decay. The beta decay can be split into beta⁻ (β^-) and beta⁺ (β^+) decay. For PET only the β^+ decay is important and therefore described in further detail.

In a β^+ decay or also called positron decay a proton converts into a neutron. Since a proton has a positive charge and a neutron has no charge the positive charge that is left after conversion cannot simply vanish according to the conservation of energy. This charge is carried away with the positron which is emitted from the nucleus in addition to a neutrino. A positron is defined as the antimatter to an electron. In eq. 2 it is described what happens to a radioactive nucleus undergoing β^+ decay.

eq. 2
$${}^A_ZX \rightarrow {}^A_{Z-1}Y + {}^0_1\beta^+ + \nu$$

X....radioactive nucleus

Y....decayed nucleus

A...mass number

Z....atomic number

β^+positron

ν ...neutrino

Then the emitted positron collides outside the nucleus with its antiparticle the electron. These two subatomic particles undergo annihilation which leads to the emission of two photons. The two photons have energy of 511keV each which is the rest mass equivalent of the particles. The path of the photons differs by 180 degrees which is the result of momentum conservation.

On their way the photons interact with matter. Depending on the energy of the photons different forms of attenuation and scatter happens such as the photoelectric effect, Compton scatter and pair building. The main contributor to scatter and attenuation for 511keV is the Compton Effect. The Compton Effect describes the interaction of a photon with an electron of an outer shell. It transfers part of its energy to the electron and therefore removes it from the atom. This is possible because the electron of the outer shell is only loosely bound to the atom with a binding energy much lower than the photon energy. The photon is then scattered and moves on a different path with an attenuated energy. Since the Compton scatter occurs most probable for energies above 100keV and below 2MeV this is the main interaction for photons with matter in PET.

2.1.2. Radiotracer

To image the decay of radioactive isotopes, it has to be combined with a biological tracer substance, yielding the so-called radiotracer or radioligand. As mentioned above the isotopes are positron emitters for use in PET imaging. The biological tracer substance is a compound with similar behavior as a naturally occurring molecule such as glucose or a neurotransmitter. Hence, the body cannot distinguish between the natural molecule and the radiotracer because of the similar physical and chemical behavior. A commonly used radiotracer is 2-[F-18]fluoro-2-deoxy-D-glucose ($[^{18}\text{F}]\text{FDG}$), a glucose analogue where an oxygen atom is substituted with a radioactive Fluor atom (^{18}F). It is used to trace the glucose metabolism which is important for e.g. tumor classification. This tracer was also used in the data of the present work. Other examples for radiotracers are $[^{11}\text{C}]\text{DASB}$ which traces the serotonin transporter or $[^{11}\text{C}]\text{-harmin}$ which binds to monoamine oxidase A. Typical isotopes used in PET are ^{18}F , ^{11}C , ^{13}N , ^{15}O and ^{68}Ga with a half-life of less than two hours. This is important to minimize the dose to the patient.

2.1.3. Data acquisition

In PET the photons which originate from annihilation have to be detected to enable reconstruction of the position of their origin. Therefore, detectors are placed in a ring around the patient. The detectors usually consist of a scintillator and a photo multiplier tube (PMT). The photon transfers its energy to the scintillator which produces visible light due to its crystal like structure. Common crystals consist of bismuth germanium oxide (BGO) or lutetium oxyorthosilicate (LSO). If the impulse is strong enough the visible light triggers the release of an electron from a photo-cathode into a vacuum filled tube where voltage is applied. The electron hits a dynode where secondary electrons are emitted. This is repeated several times to amplify the signal before the electrons reach the anode. Drawbacks of the PMTs are the low efficacy in the escape of the electron from the photo-detector and the susceptibility to magnetic fields. For a better spatial resolution the detectors are split into blocks of 8x8 elements. These blocks are then arranged in a ring where the patient is placed in its center.

PET is based on coincidence events also known as prompts. A coincidence event is detected if two photons hit two separate detectors within a certain time. Furthermore, the possibility that the photons originated from the same annihilation must be given. This can be verified by drawing an imaginary line between the detectors. If it is possible to draw a straight line within the field of view (FoV) between the two detectors the coincidence is most probably valid. This line is also called line of response (LOR) and describes the line on which annihilation took place. These events are also referred to as counts. Unfortunately not only wanted prompts are detected since there are several forms of events:

- True events are what should ideally be detected. Two photons from the same annihilation event hit the detectors within the coincidence window in an angle of 180 degrees and do not interact significantly with surrounding atoms.
- A single event happens if only one photon hits a detector, but not a second because it was either attenuated or scattered below the energy threshold of the detector or was not in the FoV anymore. These events are not considered as counts.
- A random event happens if two photons from single events reach the detectors in the coincidence window. Since the photons arise from different annihilation events a wrong LOR is assigned.
- A multiple event occurs if a single event arrives at the detector in addition to a real coincidence event with a possibly correct LOR. Since it is impossible for the scanner to distinguish which of the photons are truly from the same annihilation event this prompt is removed from the counts.

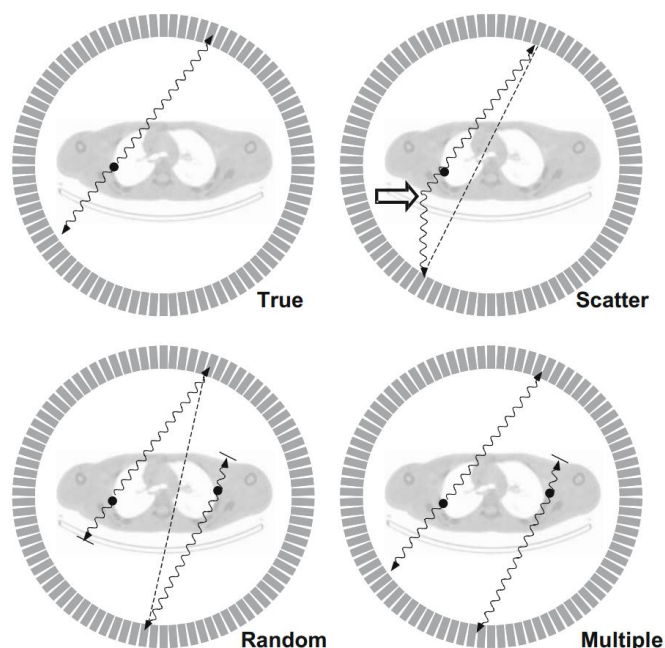


Figure 1: Annihilation event with the paths of the resulting photons. The dotted line describes the detected LOR. The illustration was taken from Bailey et al. (2004).

- Lastly, a scattered event occurs if one or both photons are scattered due to Compton interaction and the LOR does not correspond anymore to that of the originally emitted photons. Since the detector cannot distinguish between a scattered and an unscattered photon due to the low energy resolution a wrong LOR is assigned. The whole number of prompts is the sum of true, scattered and random events.

2.1.4. Image reconstruction

After the acquisition of the data the image has to be reconstructed because so far only counts were detected. Since the topic of the work is not image reconstruction the reader is referred to the literature declared in the beginning of this chapter for further details. However, an important point is the correction for scatter, attenuation, randoms and the dead time of the detectors. If these errors were not eliminated the final image would be noisy with underestimated uptake values due to the wrongly assigned LORs.

- Randoms correction

The most common method is the delayed window method. Two coincidence windows are generated. The first coincidence window will contain trues and randoms (6ns for LSO), the delayed window only contains randoms (50-56ns) because trues would reach the detector in the first window. The numbers of the random counts in the first and second window are the same within statistical fluctuations. Therefore, if the amount of counts of the second window

is subtracted from the first coincidence window only the trues will be left. A minimization of random coincidences could be reached by shortening the coincidence window since the rate of randoms is a product of length of the coincidence window and the number of singles in both detectors (see eq. 3).

eq. 3

$$R = 2\tau * C_1 * C_2$$

Rrate of randoms

τtime width of coincidence window

C_1 and C_2single count rates

- Scatter correction

Scatter occurs due to the interaction of photons with matter via the Compton Effect. The interaction occurs not necessarily only in the body of the patient but can also happen in the scintillator if not the whole energy is deposited when the photon hits the crystal the first time. Furthermore, the scatter fraction is dependent on the density and depth of the body tissue, the density of the scintillator and the activity in the patient. If the scattered events are not corrected the noise in the background is increased and the image contrast reduced since the scatter fraction can be even higher than 40%.

The correction can be done by fitting and interpolating a Gaussian function to the activity outside the source. This interpolation is then used as scatter estimation and subtracted from the measured counts. The idea of this method is that activity outside the source only originates from scatter. This process is usually done on the tails in sinogram space.

- Dead time correction

Dead time is the time where the detector cannot respond to energy deposition of an incoming photon because it is occupied by another photon. The whole dead time is from the deposition of the energy of a photon to the amplification of the signal at the end of the PMT. If a signal is incoming during this time it is not detected and therefore, no count is recorded. An example for counts not detected due to the dead time is two photons which deposit their energy of 511keV at the same time at the scintillator, overshooting the upper limit of the detector. The signal is lost.

The loss of counts increases with the activity. The amount of loss is empirically tested and then applied for correction depending on the number of counts.

- Attenuation correction

Photons get attenuated when they are travelling through tissues and organs depending on the linear attenuation coefficient (LAC). Based on the amount of attenuation of the photons the probability to detect a coincidence in a specific time window is decreased since the photon can be scattered out of the FoV or attenuated under the lower threshold of the detector. This probability can be calculated with eq. 4.

eq. 4
$$P = e^{-\sum_{i=0}^n \mu_i D_i}$$

P ...probability of coincidence detection

n ... number of tissues passed by the photon

μ_i ...LAC of the i th tissue that is passed

D_i ...thickness of the i th tissue that is passed

If the attenuation of the photons is not corrected the uptake of the final image will be too low because of lost coincidences and therefore, the quantification will be wrong.

To correct for attenuation an external radioactive source is placed in the gantry of the scanner. The idea is that the amount of attenuation can be determined by comparing the number of detected coincidences of unattenuated photons with the number of detected coincidences with an attenuating medium placed in the scanner (transmission scan). Therefore, rotating rod sources of $^{68}\text{Ga}/^{68}\text{Ge}$ are placed in the scanner as external source. The unattenuated coincidence counts are achieved by a blank scan, where no medium is in the FoV of the scanner. This scan is performed once a day and applied to all following patients. The transmission scan is carried out for every patient because of their diversity in position, size and tissue thickness to name a few reasons. Furthermore, the transmission scan exposes the patient to further radiation and further scan time of 5 to 10mins is needed for a sufficient counting statistic. Usually the scan is carried out before the radiotracer is administered. Correction factors for attenuation for each LOR can then be calculated with a division of the blank and the transmission scan.

- Normalization

The final correction that has to be made is the normalization of the detectors. Since the efficacy of hundreds of PMTs and their variation in terms of detection can fluctuate between detector pairs a correction for these issues has to be performed. This is done by a scan where all detectors are exposed to a known activity. A normalization factor can then be calculated by dividing the mean coincidence counts and the counts of a detector pair, namely their LOR

(see eq. 5). The normalization is carried out weekly or monthly due to the necessity for a long scan time of approximately 6 hours.

eq. 5
$$F_i = \frac{A_{mean}}{A_i}$$

F_i ...normalization factor for the i th LOR

A_{mean} ...average coincidence events of all LORs

A_i ...number of counts of the i th LOR

An illustration of the path of the image reconstruction can be seen in Figure 2.

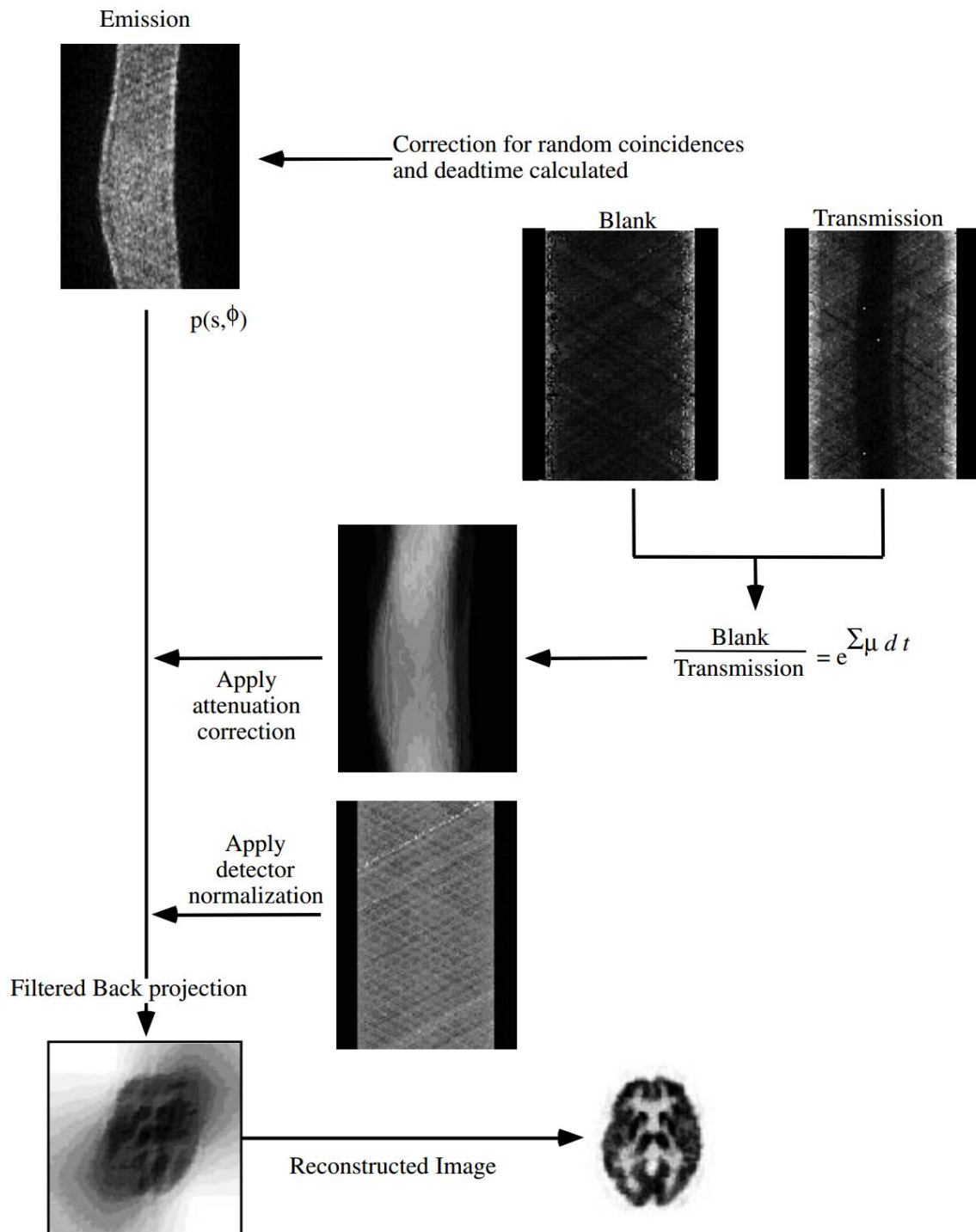


Figure 2: For a quantitatively correct reconstructed image the data has to be corrected for randoms, scatter, dead time and attenuation. The attenuation correction is carried out with a blank and transmission scan with an external radioactive source. Factors from detector normalization have to be applied due to the difference performance of the PMTs. The emission and attenuation correction data are represented as sinograms. The image was taken from Bailey et al. (2004).

2.2. Hybrid PET/CT scanners

Hybrid PET/CT scanners consist of a CT and a PET scanner, sequentially arranged. These scanners were invented for a faster and better detection of tumors and the possibility to fuse the PET and CT image for improved anatomical localization. Furthermore, the CT is used for attenuation correction (AC). Thus, no further registration is necessary of the data because the patient stays in the same position on the bed for the whole scan. The acquisition is acquired sequentially, first the CT scan is performed, thereafter the PET scan. The setup of this hybrid system is equal to the previously described except stand-alone PET, except for the rotating rod sources which are replaced by the CT.

As already mentioned assets of a hybrid PET/CT scanner are the faster and more accurate detection of tumors and the possibility to fuse the images of the different modalities. Furthermore, the AC of the PET/CT can be acquired within seconds while the transmission scan with rotating rod sources takes several minutes. This leads to a higher comfort to the patient and an increased throughput of the scanner which is important for the clinical routine.

A drawback of the PET/CT scanner is that the LACs of the CT are given in Hounsfield units (HU) which do not correspond to the LACs for 511keV. Therefore, the AC cannot directly be applied to the PET scan. A CT scanner is rotating around the patient emitting x-rays. These x-rays are interacting with matter of the patient before they reach the detector. Differently to 511keV photons x-rays mainly interact via the photoelectric effect because of their lower energy of around 120 to 140 keV. The photoelectric effect describes the interaction of photons with electrons of the inner shell of an atom. The incoming x-ray photon knocks out the electron by transferring its whole energy minus the binding energy to the electron as kinetic energy. The original photon vanishes. The hole is then filled by an electron from an outer shell, emitting characteristic x-ray radiation.

To adjust the LACs for x-ray to 511keV a bilinear scaling is usually applied (Carney et al. 2006). The first linear scaling is applied to the HU of air, water and soft tissue. Because of different behavior of bone, the greatest contributor to photon attenuation, the second linear scaling has to be applied to the remaining values.

Another drawback is the starvation of low energy photons on metal implants. These metal implants absorb the x-rays but are transparent to a different extent for 511keV photons. Therefore, a scaling for HU of metal implants is not possible and leads to wrong AC.

Although the scaling is not as accurate as the AC of the usual PET the assets predominate and therefore, hybrid PET/CT scanners replace normal PET scanners in most clinical settings.

2.3. Hybrid PET/MR scanners

A rather new hybrid scanner is the PET/MR which consists of an MR gantry combined with PET detectors, i.e., the PET part is directly integrated into the MRI scanner. The detectors are inserted between the MRI gradient and body coils which makes a simultaneous acquisition of MR images and PET emission data possible (Delso et al. 2011). A drawback of the hybrid PET/MR system is that AC cannot be directly performed MR is not capable of detecting attenuated photons. In a PET-only system AC is performed with an additional radiation source, in PET/CT scanner AC is carried out with a CT where HUs are scaled to 511keV. Differently, it is impossible to depict bone in MR images due to its density even though it is the greatest contributor to photon attenuation. The reason for the lack of bone in the images is inherent to the technique of MR imaging.

2.3.1. MRI

In MRI the majority of sequences are focused on the hydrogen atom, more precisely on the proton in the nucleus. A strong static magnetic field B_0 of 3 to 7 Tesla is set. This leads to a parallel or antiparallel orientation of the protons to the magnetic field. A subject in the scanner is then exposed to radio frequency pulses which deflect the protons. The reorientation to the initial static field leads to changes in local magnetic field properties of the tissue which can be sampled and an image reconstructed. Depending on the time point of the sampling differently weighted images can be obtained leading to different contrast between different tissue types. For instance, if the repetition time of the radio frequency impulse is short and also the sampling happens shortly after the emitted radio frequency impulse a so called T1-weighted images is produced. A T1-weighted image describes the longitudinal relaxation time which is also called spin-spin relaxation time. A long repetition time and also a long echo time leads to a T2-weighted image which is based on the transversal relaxation time of the deflected protons. In terms of the brain a T1-weighted image shows a higher intensity for white matter whereas a T2-weighted image has higher intensity in the gray matter. Bone is not visible in both cases. The reason is the low water content in dense bone and therefore, the small number of hydrogen atoms which are needed for common MR imaging (Stoecker et al. 2007).

2.3.2. Challenges

Because of the magnetic field special electronics have to be installed which must not be sensitive to the field. Therefore, it is impossible to use the usual detectors with PMTs because of their susceptibility to the magnetic field. The Lorentz force deflects affected electrical charges such as electrons. Hence, electrons would not reach the anode of the PMT and no electrical signal could be amplified. Thus, PMT detectors are replaced with solid state

scintillation detectors such as avalanche photo diodes (APDs). A photon hits the scintillator which produces electron-hole pairs in the detector. An electric field is applied and leads to a flow of charge. This flow is amplified and can be measured as charge which leads to the detection of photons. A disadvantage is their sensitivity to temperature which leads to charge flow on higher temperatures and their lower gain. Advantages are their smaller size for a better placement and their insensitivity to magnetic fields (Pichler et al. 2008). A comparison of the detectors and their sensitivity to magnetic fields can be seen in Figure 3.

In the case of the Siemens Biograph mMR, which is also mounted at the General Hospital of Vienna, APD-lutetium oxyorthosilicate detectors were installed (Delso et al. 2010).

Another challenge which was already mentioned is the AC. Since no transmission scan can be performed other approaches are required. The gold-standard for research studies is the acquisition of a low-dose CT on a different scanner. Drawbacks of this approach are the additional radiation exposure for the patient, the logistic issue and the need for further processing such as coregistration. Therefore, other approaches were invented with varying success. The most common methods are segmentation based approaches of a structural T1-weighted image but also atlas-based approaches exist with MR-CT pairs. The comparison of their efficacy compared to the gold standard CT is part of this work. The greatest issue is to detect the non-depicted bone in the MRI.

2.3.3. Assets

Although there are still issues that have to be resolved the PET/MR is an improvement to the PET/CT and also the PET-only system. If the issue with AC can be solved the radiation

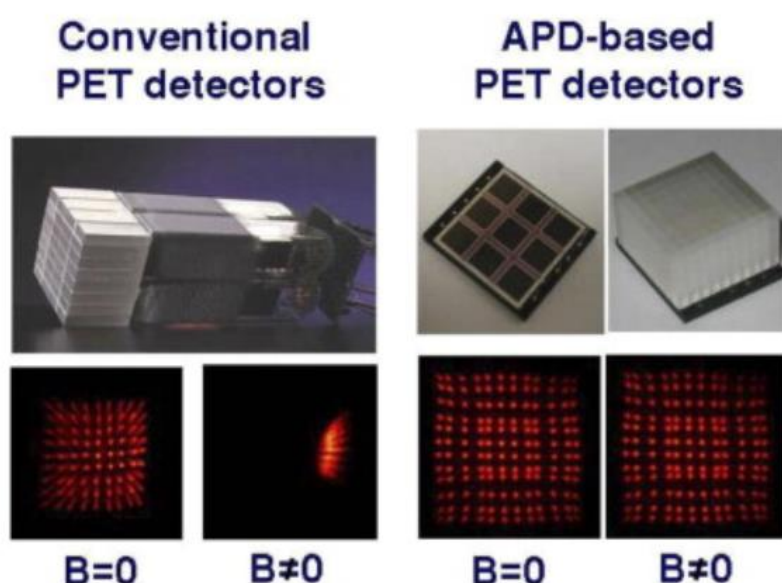


Figure 3: The conventional detectors in PET are PMTs (left) whereas APDs are used in PET/MR (right). The lower images show detector element maps. On the left it can be seen that the PMT detectors are sensitive to a magnetic field. A small horse magnet was placed near the detector. Differently, the APD-based detector map is not affected by a magnetic field, not even for 7T. Image taken from Pichler et al. (2008).

exposure of the patient can be minimized and the comfort of the patient can be increased since no low-dose CT scan has to be performed. Furthermore, the logistical issue of transferring the patient between the scanners and also the need for the preprocessing of the CT disappear.

The biggest asset is the possibility of simultaneous MRI and PET acquisition. Thus, functional MRI and PET can be coupled and evaluated together which might have a huge impact on future research studies. Due to the simultaneous recording the images are in perfect alignment. Therefore, the MRI can easily be fused with the PET image for a better orientation and a more reliable diagnosis in the clinical routine.

3. Methods

3.1. Population

The subject data used in this work originated from a different completed study about quantification with constant infusion of [^{18}F]FDG (Hahn et al. 2016) at the Medical University of Vienna where 18 right-handed healthy subjects were scanned. After the explanation of the study protocol all subjects gave written informed consent. The study was supported by a grant of the Austrian Science Fund (FWF KLI 516) and was approved by the ethics commission of the Medical University of Vienna (ethics number: 1916/2013)

For this retrospective work one of the 18 subjects had to be excluded due to a missing CT leading to a subject size of 17 (mean age \pm SD = 24.6 \pm 4.2, 8 female).

3.2. Measurement

At the screening visit all subjects underwent standard medical examination including blood and psychological tests and electrocardiography to rule out pre-existing physical and mental disorders. Female participants had to take a pregnancy test right before each PET scan.

Thereafter, all subjects were once scanned for 100 minutes on a Siemens Biograph mMR hybrid PET/MR system (Siemens Healthcare, Erlangen, Germany).

To image and to quantify glucose metabolism the radioligand 2-[F-18]fluoro-2-deoxy-D-glucose ([^{18}F]FDG) was administered. The tracer was constantly infused through the cubital vein for 95 minutes at a rate of 36 ml/h. Target dose was 3MBq/kg which leads to an effective dose of 4.275 mSv for a person with 75kg.

Three different conditions were measured:

- In an eye open condition subjects had their eyes opened. (10 – 20mins, 60 – 70mins)
- In a finger tapping condition subjects repeatedly tapped their thumb of the right hand to the fingers while the eyes were closed. (35 – 45mins, 85 – 95mins)
- A baseline condition was added between the tasks where subjects had their eyes closed and were not allowed to fall asleep or think about difficult tasks.

For the evaluation of the performance of the different attenuation correction approaches the mean was calculated for the time course of 40 – 60mins (for further details see chapter 3.6). The different conditions were neglected because the task-specific change of the glucose metabolism in specific brain regions is not of relevance for this study. Similarly, for the methodological assessment and comparison of different AC methods, it is not relevant if

standard uptake values or the cerebral metabolic rate of glucose (CMR_{glu}) is used as outcome parameter.

Since the Biograph mMR can be operated in PET- and MRI-mode simultaneously MR images were acquired during PET acquisition, including a T1-weighted structural MRI (magnetization-prepared rapid gradient echo (MP-RAGE), TE/TR = 4.2/2000ms, voxel size = 1 x 1 x 1.1mm).

Additionally all subjects underwent one low-dose CT scan (120 kVp, voxel size: 0.5859x 0.5859 x 1.5 mm) on a Siemens Biograph TPTV PET/CT (Siemens MI, USA) for AC. Furthermore, 15 out of 17 patients underwent at least one measurement on a GE Advance PET Scanner (General Electric Medical Systems, Waukesha, WI, USA) for 60 or 95 minutes. For this work only the transmission scan of the subjects was of interest.

3.3. Attenuation correction

Although the CT currently represents the most suitable AC its acquisition requires an additional scan as well as processing such as coregistration. Therefore, other methods are highly desirable for the clinical routine and also for research studies. The approaches used in the current evaluation are the gold-standard and reference CT, an atlas-based approach (pseudoCT), two segmentation-based approaches provided by the vendor (DIXON, UTE) and, the theoretical gold-standard, the transmission scan from the GE-PET.

3.3.1. Attenuation correction with CT

A low-dose CT scan was recorded for all subjects for AC. However, before the CT could be used as AC map it had to be preprocessed:

The files of the CT were converted from the standardized "Digital Imaging and Communications in Medicine" (DICOM) format into the format specified by the Neuroimaging Informatics Technology Initiative (NifTI) (<http://nifti.nih.gov>). Thereafter, the CT was cut so that only head, neck and neck holder were present in the image without the shoulders. Furthermore, the T1-weighted MRI and the DIXON AC map (DIXON is an AC map based on MR, provided by the vendor and will be described later) were converted from DICOM to NifTI as well using the dcm2nii tool provided by Chris Rorden (<http://people.cas.sc.edu/rorden/mricron/dcm2nii.html>). The orientation of the CT, MRI and the DIXON AC map remained the same before and after the format conversion.

Next, the CT had to be brought into the same position as the PET of the PET/MR for correct AC since it was recorded on a different scanner. Therefore, it was assumed that the PET and MR image were in perfect alignment, due to their simultaneous recording, and coregistered

the CT to MRI with normalized mutual information. This was done with the MATLAB software package “Statistical Parametric Mapping” SPM12. For later steps and correct orientation of the AC map the coregistered CT was then resliced to DIXON image space (matrix size 192 x 126 x 128, voxel size 2.6042 x 2.6042 x 3.12 mm).

The neck holder had to be removed because it is only present in the PET/CT scanner but not in the PET/MR system and would therefore lead to erroneous AC. It was removed by creating a mask with thresholding. To preserve the information in the CT air holes in the mask were filled before all voxels around it were set to -1024, the HU value for air. In cases where the CT image did not cover the whole head and neck region the area was substituted with voxels from the AC DIXON so that the reconstruction algorithm could perform correct scatter correction.

The result of these steps was a CT image in NifTI format correctly positioned and orientated without the neck holder.

As described in the chapter *Physical Background*, CT scans are recorded in Hounsfield units (HU), a measure for x-ray attenuation, which is not applicable for PET scans. Therefore, the CT image matrices were scaled bilinearly to convert from HU to the photon energy of 511keV. Bilinear scaling was chosen because it could be shown that it represents a valid model for conversion (Carney et al. 2006). HU values below 70 HU were scaled according to eq. 6, HU values above or equal to 70 are scaled according to eq. 7, the reference value was 120kVp (Carney et al. 2006). Values below zero were set to zero since negative attenuation is not possible in this case.

$$\text{eq. 6} \quad HU < 70: \quad (9.5 * 10^{-5}) * (HU + 1000)$$

$$\text{eq. 7} \quad HU \geq 70: \quad 5.1 * 10^{-5} * (HU + 1000) + 4.7 * 10^{-2}$$

Furthermore, the linear attenuation coefficients (LAC) representing the tissue density distribution (Keereman et al. 2010) for 511keV had to be multiplied with 10^4 because the Siemens reconstruction software expects the LACs in the unit μm^{-1} while the unit in the CT image is in cm^{-1} . In the actual reconstruction step the software rescales the linear attenuation coefficients back to cm^{-1} .

Lastly, before the CT could be used as AC map, it was converted back to DICOM format. Since there is, to our best knowledge, no standard program which is able to convert from NifTI to DICOM format directly data was first transformed to MINC format and then to DICOM. For the conversion from MINC to DICOM the information in the Dixon DICOM files was used as template and only the DIXON image matrix values were substituted with the ones of the CT (matrix size: 192 x 126 x 128, voxel size: 2.6042 x 2.6042 x 3.12mm).

The whole process was fully automated except for the removal of the shoulders and realized in Bash and MATLAB. NifTI toolbox, SPM12 and MINC were used as toolboxes.

The processing steps from the original CT to the AC CT can be seen in Figure 4 in a simplified flow chart.

Attenuation Correction in PET/MR Brain Imaging

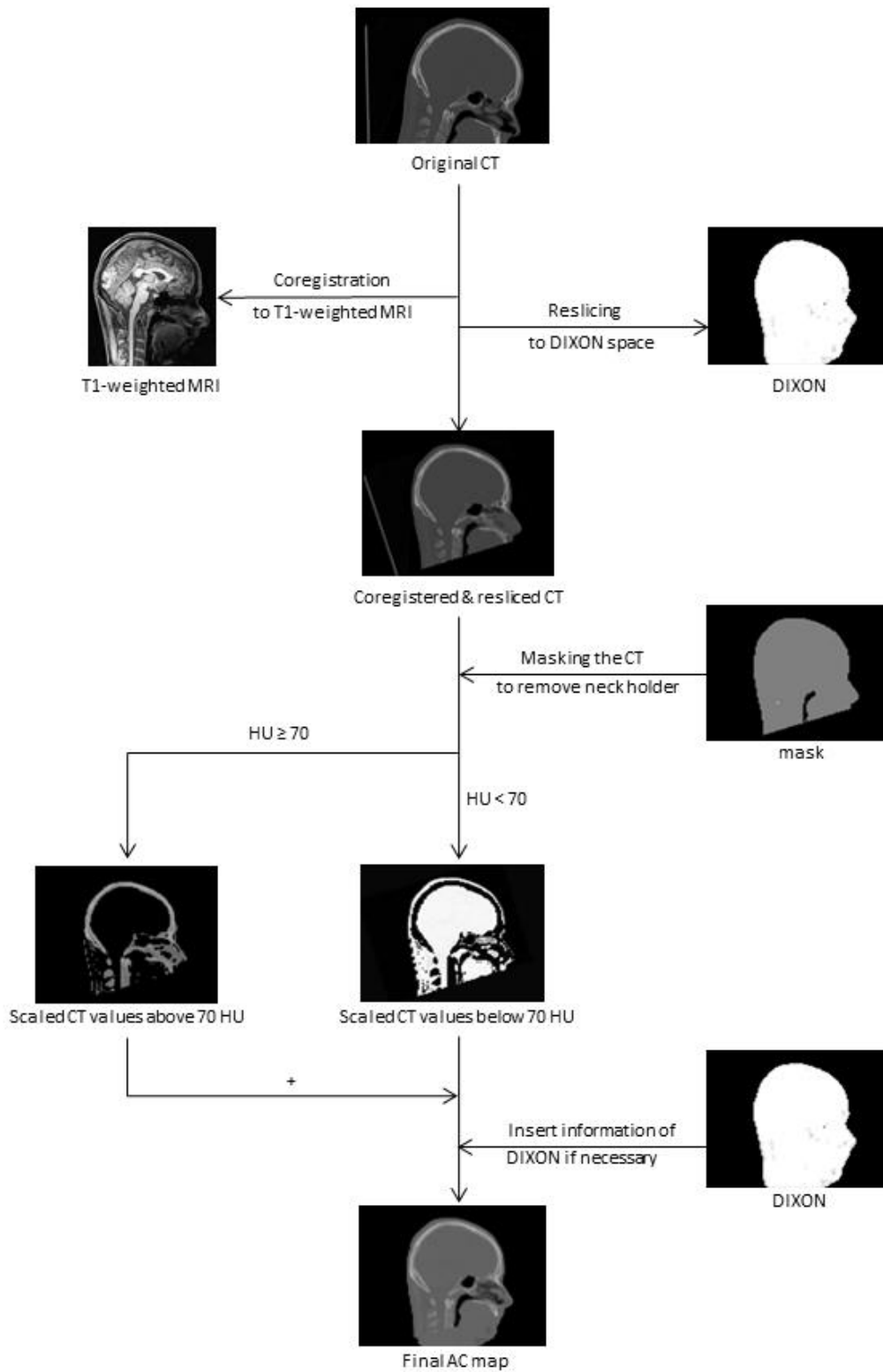


Figure 4: Simplified flow chart of the processing steps from the original CT to the final AC CT

3.3.2. Attenuation correction with pseudoCT

To substitute the CT scan another approach was invented by (Burgos et al. 2014) from the University College London where an individual T1-weighted target MRI is converted to an atlas based synthetic CT (pseudoCT).

The authors established an atlas database filled with preprocessed coregistered CT-MRI pairs, meaning for every MRI there is a corresponding and aligned CT scan of the same subject. Preprocessing included removal of the neck holder for the CT using thresholding and morphological operations as well as correction of image intensity bias for the MRI.

For the conversion from MRI to pseudoCT all MRIs of the database were first coregistered with normalized mutual information to the target MRI. Then the resulting transformation matrices were applied to the corresponding CTs of the atlas database so that all CTs were in alignment with the target MRI. Next, they investigated the correlation of the local image intensities between the target MRI and the coregistered set of MRIs. Since it was assumed that local similarities are in correspondence with local morphological similarities between subjects the similarities were transformed into weighting factors. Higher similarities led to higher weights. These values were applied to the calculation of the weighted mean of all CTs in the database which resulted in the final pseudoCT (Burgos et al. 2014).

Furthermore, the University College London provides a website (<http://cmictig.cs.ucl.ac.uk/niftyweb/program.php?p=PCT>) to transform a target MRI to a pseudoCT. A T1- or T2-weighted target MRI has to be uploaded in NifTI format. It is possible to choose between optimization for accuracy or speed, depending on the preferences. For this work, optimization for accuracy was chosen and thus, after approximately 2 hours the resulting pseudoCT was returned to the provided e-mail address in NifTI format (see Figure 5 and Figure 6). As the final step the pseudoCT was scaled and treated in the same manner as the CT to obtain an AC map from the pseudoCT.

3.3.3. Attenuation correction with segmentation approaches

The following AC maps are created by segmentation of MRI images as provided by the vendor and can be distinguished by means of their techniques:



Figure 5: Structural T1-weighted target MRI uploaded to the provided website of the University College London

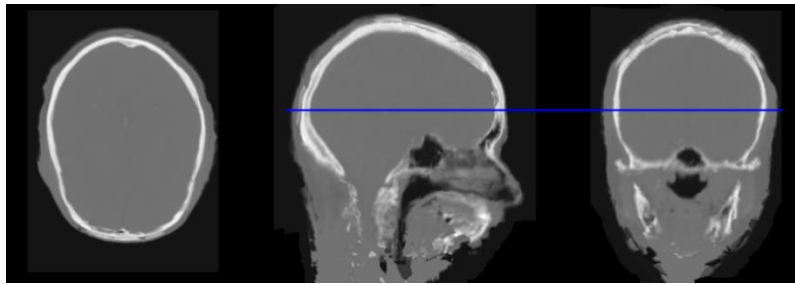


Figure 6: Returned pseudoCT which results from the provided target MRI (see Figure 5), optimized for accuracy

3.3.3.1. Attenuation correction with DIXON

As previously described it is impossible to distinguish air from bone with common structural MRI sequences because of the low water content and the fast transverse relaxation time of bone. Therefore, an approach based on MRI fat and water image segmentation was invented, incapable of detecting bone tissue. This approach was implemented by the vendor and is called DIXON. The AC map is based on a two point DIXON volume-interpolated-breath-hold-examination (VIBE sequence) technique with echo times where fat and water spins are in or out of phase with each other due to their different resonance frequencies. With dual gradient echo times these images can be acquired within one sequence ($TE_1/TE_2/TR = 1.23\text{ms}/2.46\text{ms}/3.60\text{ms}$, flip angle = 10°). From the in- and opposed-phase images fat and water images can be estimated (<http://mri-q.com/dixon-method.html>, retrieved on 2016-08-16):

eq. 8
$$W + F = IP$$

eq. 9
$$W - F = OP$$

eq. 10
$$\left(\frac{1}{2}\right) * (IP + OP) = \left(\frac{1}{2}\right) * [(W + F) + (W - F)] = \left(\frac{1}{2}\right) * (2W) = W$$

eq. 11
$$\left(\frac{1}{2}\right) * (IP - OP) = \left(\frac{1}{2}\right) * [(W + F) - (W - F)] = \left(\frac{1}{2}\right) * (2F) = F$$

IP ... intensity in-phase

OP ... intensity opposed-phase

W ... intensity water

F ... intensity fat

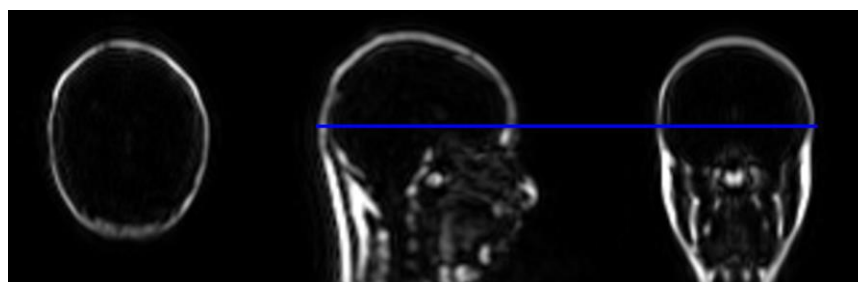


Figure 7: Fat image calculated from the in- and opposed-phase images, produced by the Siemens Biograph mMR scanner

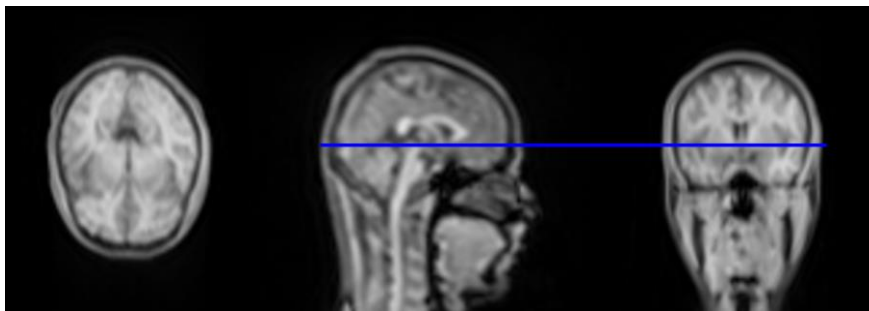


Figure 8: Water image calculated from the in- and opposed-phase images, produced by the Siemens Biograph mMR scanner

Since there is no documentation how calculation is actually carried out by the PET/MR system this was manually checked. Water and fat images were calculated from the *IP* and *OP* images from the scanner and compared to the scanner output where almost identical results were obtained. Differences were only found in the neck region.

Then the fat and water images were thresholded for segmentation into compartments for soft tissue, fat and air with the LACs $1000 \mu\text{m}^{-1}$, $854 \mu\text{m}^{-1}$ and $0 \mu\text{m}^{-1}$, respectively (Martinez-Möller et al. 2009). In whole body studies also lung is a compartment. The final Dixon AC map is generated by the PET/MR scanner in DICOM format with a matrix size of $192 \times 126 \times 128$ and a voxel size of $2.6042 \times 2.6042 \times 3.12 \text{ mm}$.

However, a drawback of this approach is that inconsistencies in the generated AC map may occur. In 28% of all subjects of the original study a so called tissue swap happened. In a tissue swap the scanner uses the fat image as water image and vice versa for segmentation which leads to misclassifications of soft and adipose tissue. Since the algorithm of the scanner for the generation of the AC map is unknown it is not comprehensible how the error occurs. Another drawback is the susceptibility of the MR to metal which cancels the signal, for example retainers. It is impossible for the scanner to detect the retainer therefore treating the area wrongly as air/background (see Figure 9).

3.3.3.2. Attenuation correction with UTE

Another approach which was also implemented by the vendor is the segmentation of MRI images acquired with an ultra-short echo time sequence (UTE). Since there is again no

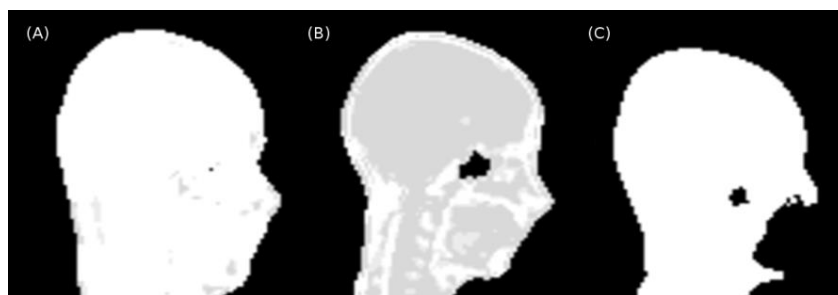


Figure 9: (A) correct DIXON (B) DIXON with fat, water tissue swap (C) correct DIXON with cancelled signal in the area of the mouth, due to a retainer. Soft tissue, fat and air are depicted in white, gray and black, respectively.



Figure 10: Result of the segmentation of the R2 map as obtained from the scanner with bone in white, soft tissue in gray and air in black

documentation on how this approach was implemented by Siemens it was assumed that it is based on the work of (Keereman et al. 2010). Common MRI sequences sweep the signal at a time point where cortical bone signal has already disappeared due its fast transverse relaxation time constant (T_2) and therefore, its fast transverse relaxation rate (R_2). Originally, ultra-short echo times were invented to image tissues with a short T_2 like tendons or ligaments. Although the T_2 of bone is even shorter, the authors used UTE to generate an AC map from this signal. They used a dual gradient echo with slightly different parameters compared to the Siemens PET/MR system due to different technical premises (Siemens PET/MR implementation: $TE_1/TE_2/TR = 0.07/2.46/11.94\text{ms}$, flip angle = 10°). From the two acquired MRI images a R_2 map was calculated (eq. 12):

$$\text{eq. 12} \quad R_2 = \frac{\ln I_1 - \ln I_2}{TE_2 - TE_1}$$

Since the R_2 describes the inverse of the spin-spin relaxation time T_2 high values were expected for cortical bone whereas soft tissue should have low R_2 values. With these R_2 values it becomes possible to distinguish between bone and soft tissue. However, the authors report a greater difficulty to differentiate between air and bone because of high R_2 values for air arising from artifacts. Thus, they smoothed the R_2 map and applied a mask setting all voxels containing air to zero. The corrected R_2 map is then segmented into bone, soft tissue and air, with the linear attenuation coefficients $1510 \mu\text{m}^{-1}$, $1000 \mu\text{m}^{-1}$ and $0 \mu\text{m}^{-1}$, respectively, resulting in a UTE AC map (matrix size $192 \times 192 \times 192$, voxel size $1.5625 \times 1.5625 \times 1.5625\text{mm}$).

It is important to note that although this AC approach is also MR and segmentation based it differs from the DIXON approach since it segments bone instead of adipose tissue.

3.3.4. Attenuation correction with transmission scan

The last approach we compared to the AC CT approach was the transmission (TX) scan. As described previously in the chapter *Physical Background*, rotating $^{68}\text{Ge}/^{68}\text{Ga}$ rod sources are mechanically moved in front of the PET detectors. Due to annihilation, coincidence events are then acquired by the detector behind the rod sources and the detector in the opposing fan. Thus, an attenuation profile for photons with 511keV can be estimated without the necessity of further scaling such as in the case of CT (Bailey 1998).

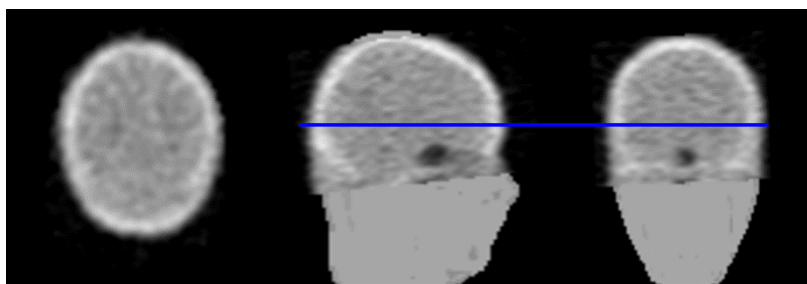


Figure 11: Transmission scan transformed to AC map with AC DIXON attached to area without information. Bone is clearly visible in white, soft tissue in gray. It can be seen, that the center of the head has similar LACs compared to the neck region of the AC DIXON, namely soft tissue.

Since 15 subjects underwent at least one PET scan TX maps were also available for these subjects as the TX maps are used for AC in the PET scanner and always recorded. The TX maps were acquired for 5 minutes before the scan and before tracer application (voxel size $4.2969 \times 4.2969 \times 4.25$).

The TX scans had to be preprocessed before they could be used for AC. First, the neck holder was removed by hand in MRicron (<http://people.cas.sc.edu/rorden/mricron/>) by masking it and setting all voxels around the head to -1024, the HU value for air. Then, the TX map underwent the same procedure as the CT but without the removal of the neck holder and the bilinear scaling. Instead, LACs smaller than zero were set to zero and then scaled with 10000 from cm^{-1} to μm^{-1} . Bilinear scaling was not necessary because the LACs in the TX map already correspond to photons with energy of 511keV. Due to the smaller field of view of the TX scan the DIXON AC map was used in areas without TX signal (see Figure 11).

3.4. Image reconstruction

Since the data is recorded not in a final viewable image but rather in a format which only stores events, named Listmode, the patient emission data has to be reconstructed. The reconstruction was done with JSRecon12 and e7-tools provided by Siemens and consisted of 4 steps:

1) Adapting the parameter file

The parameter file comprises all parameters which are important for reconstruction. The standard Siemens parameters were used except for the postfiltertype (von Hann instead of Gauss) and an Ordinary Poisson – ordered subset expectation maximization algorithm (OP-OSEM) with 3 iterations and 21 subsets was chosen. Since listmode only stores events it offers the opportunity to reconstruct the data at arbitrary frame lengths retrospectively. Thus, the parameter file was changed so that 100 frames, 1 frame per minute was created.

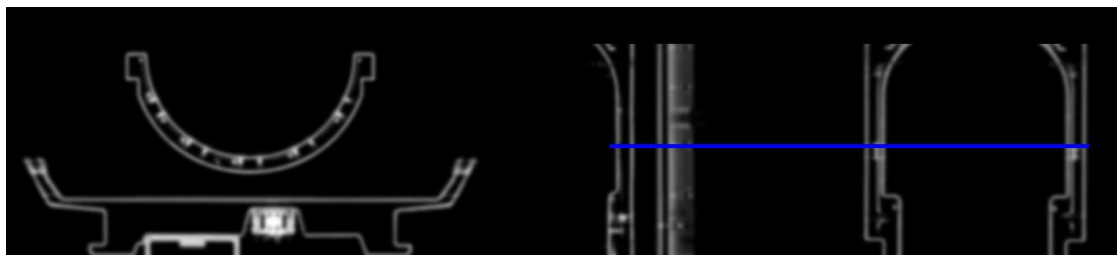


Figure 12: Hardware AC map of the bed and head coil

The next 3 steps were carried out with batch files generated by JSRecon12. These batch files call e7-tools commands:

2) Histogramming

Histogramming splits the whole listmode emission data into the chosen frame lengths and creates sinograms for the corresponding times.

3) Applying the OP-OSEM algorithm

In this step the OP-OSEM algorithm is reconstructing the frames, incorporating the parameters specified in the parameter file. The previously described AC maps are now applied, one AC map per reconstruction. Since the hardware also attenuates the signal before it reaches the detector it has to be taken into account as well. These hardware AC maps (Figure 12), e.g. the head coil, are provided by the vendor and used automatically by the reconstruction software. Furthermore, scatter, dead time and random corrections are performed and the normalization file is used.

4) Interfile to DICOM conversion

Finally the produced Interfile format is translated to the DICOM standard and the DICOM tags are filled with information from the reconstruction and the original listmode file.

The reconstruction process leads to an output of 12700 DICOM files, 127 files per frame, one file per slice and takes approximately 8 hours for 100 frames. The whole three dimensional volume has a matrix size of $344 \times 344 \times 127 \times 100$ and a voxel size of $2.0863 \times 2.0863 \times 2.0313\text{mm}$.

3.5. Image preprocessing

After the reconstruction the viewable images have to be preprocessed due to the natural diversity of brains. This diversity has to be minimized so that all brain regions of all subjects are in the same position to be able to compare the results between the subjects. This was achieved by the following preprocessing steps:

- Spatial realignment

The idea behind spatial realignment is to reduce the movement between the frames since, during 100 minutes it is possible and probable the subject moves its head. Without the movement correction the quantification would be wrong due to the fact that the brain regions would not be in the same position during the whole scan. Therefore, the reconstructed DICOM files were visually checked for movement in PMOD (<http://pmod.com>) before they were converted to the NifTI format. A mean image was calculated from the longest time series without movement. The final spatial realignment was performed for all frames in a two-pass procedure: the first pass was an alignment to the previously calculated mean, the second pass an alignment to the mean of the whole time course. The transformation model used was a six parameter rigid body transform model (3 translations, 3 rotations). The estimated transformation matrix was not applied to the PET data but rather saved and used for the further steps to keep interpolations and inherent smoothing caused by reslicing at a minimum.

It should be noted that after reconstruction movement correction can only be performed between the frames but not within frames.

- Coregistration

As a preprocessing step for the spatial normalization the PET data was coregistered to the recorded structural T1-weighted MRI although, they should theoretically already be in perfect alignment as a result of their simultaneous acquisition. The coregistration was performed with normalized mutual information. Again, the transformation matrix was not applied but saved and used in the normalization process.

- Normalization

The next preprocessing phase is the spatial normalization. A nonlinear deformation field is estimated which fits tissue probability maps on the structural T1-weighted MRI. The T1-weighted image is used instead of the PET frames because of the higher spatial and better morphological resolution which makes this step more reliable. Since the MRI and the PET are in alignment after coregistration, the nonlinear deformation field of the MRI can be applied to the PET. Within this step the previously estimated transformation matrices are written to the PET images as well. The final normalized PET frames are in Montreal Neurological Institute (MNI) space, a standard brain, with a matrix size of $79 \times 95 \times 79$ and an isotropic voxel size of 2mm. Finally, the brain regions of all subjects should be at the same position and can be compared in future processes.

All preprocessing steps were carried out in SPM12 with standard parameters. Furthermore, all estimations were only performed once per subject and applied to all reconstructions. Therefore, intrasubject variabilities arising from preprocessing steps should be negligible.

3.6. Image postprocessing and statistics

After the preprocessing the data was further processed for the final analyses. A mean image was calculated of a 20 minutes time course, corresponding to 40 to 60 minutes. This time range was selected due to similar time courses in previous works (Mosconi et al. 2009; Chung et al. 2002; Ishii et al. 2001; Lee et al. 2008) and for a better signal to noise ratio.

The standard uptake value (*SUV*) was calculated for each voxel of the mean maps in accord with eq. 13 to normalize the voxel values for the feasibility of comparison between the subjects. Mean *SUV* values of 98 regions of interest (ROIs) of an Automated Anatomical Labelling (AAL) atlas (Tzourio-Mazoyer et al. 2002) were read out for all reconstructions of all subjects.

$$\text{eq. 13} \quad SUV = \frac{\text{PET image concentration}}{\frac{\text{injected dose}}{\text{body weight}}}$$

The reconstructions were grouped according to their AC approach. Nonetheless, due to the tissue swap, DIXON and TX (influenced by the DIXON tissue swap because of the small field of view) had to be further subgrouped resulting in the following groups:

- CT (n = 17)
- pseudoCT (n = 17)
- DIXON including all subjects (DIXON_{all}, n = 17)
 - DIXON including only subjects with DIXON tissue swaps (DIXON_{ts}, n = 5)
 - DIXON including only subjects with correct DIXON AC map (DIXON_{ok}, n = 12)
- UTE (n = 17)
- TX including all subjects which underwent a PET scan (TX_{all}, n = 15)
- TX including only subjects with DIXON tissue swaps (TX_{ts}, n = 5)
- TX including only subjects with correct DIXON AC map (TX_{ok}, n = 10)

The evaluation of the differences between the reconstructions with the AC CT and the other groups were carried out on an ROI and voxel-wise basis.

Linear regression analysis was performed for all groups with respect to CT to assess similarity between the CT and alternative approaches (r^2 , slope and intercept). Scatter and Bland-Altman plots should reveal differences in a graphical domain. The plots were created for all groups and all 98 ROIs.

Furthermore, for the voxel-wise analyses difference maps were calculated between the *SUVs* reconstructed with AC CT and all other approaches. For comparison with previous studies, the mean error of the whole brain was calculated from the difference maps after masking the brain. Additionally, to test the differences for significance paired t-tests were performed in SPM12 where $p < 0.05$, FWE corrected for multiple comparisons was considered significant.

4. Results

The aim of this study was to figure out the performance of various AC methods and the possibility to substitute the CT to decrease the radiation exposure to the patient while sustaining the accuracy of the quantification. Therefore, the following subsections show the performance of the AC approaches compared to the CT.

4.1. Attenuation correction with pseudoCT

Since the pseudoCT is a mean CT from an atlas database simulating an individual CT it should theoretically perform as good as the real AC CT. A scatter plot on the left of Figure 13 shows that the ROIs with the $SUVs$ of the reconstruction with AC CT (SUV_{CT}) and the reconstruction with AC pseudoCT ($SUV_{pseudoCT}$) are in high correlation ($r^2 = 0.99$). Furthermore, the regression line (slope = 1.02, intercept = -0.05) is almost in accordance with the line of identity which indicates that SUV_{CT} and $SUV_{pseudoCT}$ are performing almost identically. The Bland-Altman plot on the right of Figure 13 supports the finding in the scatter plot since all values are very close to the center at -0.015. However, the center below 0 reveals a slight underestimation of the $SUVs$ from the reconstruction with AC pseudoCT. Since the underestimation is so small on an ROI bases it might can be neglected.

In addition to the ROI-based comparison a voxel-wise analysis was carried out by calculating a difference map between the SUV_{CT} and $SUV_{pseudoCT}$. In Figure 14 the difference map shows an error of up to 4% in occipital and brainstem regions and an error of up to 10 to 15% in lateral and frontal regions close to the bone. Errors higher than 30% are found outside the gray matter and are not of relevance for this work. The mean error across the whole brain was 2.66%.

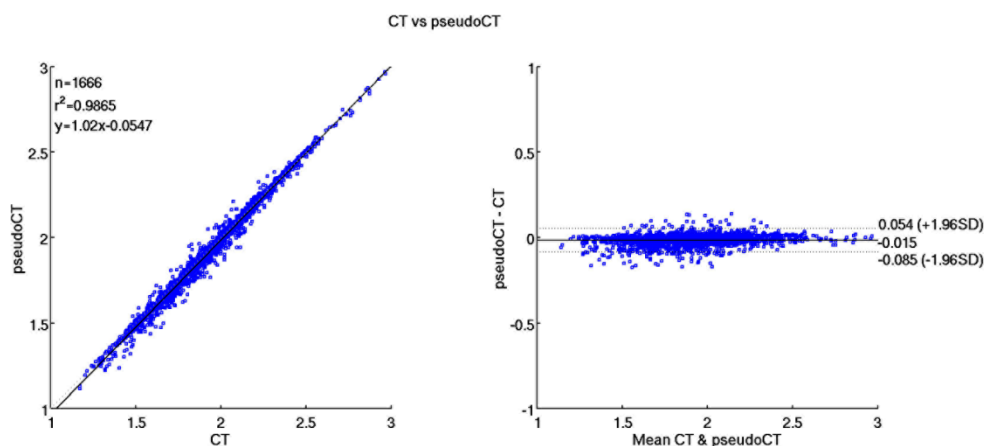


Figure 13: ROI-based correlation between $SUVs$ of the reconstruction with AC CT and AC pseudoCT (left). The scatter plot shows high correlation ($r^2 = 0.99$), a slope of almost 1 and an intercept near 0, indicating a similarity of the $SUVs$ and also of the AC maps to a great extent. The Bland-Altman plot (right) shows a small fluctuation margin around the center at -0.02 revealing a slight underestimation for the values reconstructed with AC pseudoCT. Therefore, the similar performance of both AC approaches is also supported by the Bland-Altman plot.

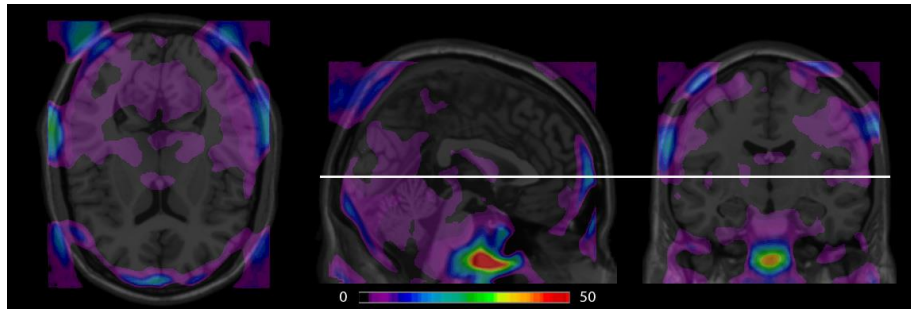


Figure 14: Voxel-wise difference map in percent between $SUVs$ reconstructed with AC CT and AC pseudoCT. The difference map shows small differences up to 4% in occipital regions and a difference of around 10-15% in frontal and lateral regions close to bone tissue. Errors above 30% are outside of the brain and can be ignored for this work.

To evaluate if the differences found in Figure 14 are significant a paired t-test was performed comparing SUV_{CT} with $SUV_{pseudoCT}$. The statistical result is shown in Figure 15 and demonstrates significant differences with T-values above 8.59, $p < 0.05$ FWE corrected. With this threshold only the variation in the lateral regions remains indicating that the small errors in the occipital and frontal regions are not significant.

The small fluctuations on a voxel-wise but also on an ROI basis indicate that the calculation of the AC pseudoCT from an atlas depicts bone and soft tissue correctly leading to a correct photon attenuation and scatter profile. However, regions which are highly different for individuals such as the frontal sinuses are hard to model from mean CTs and therefore, lead to higher errors in the difference maps. Thus, it is dependent on the individual scientific question if the errors of the difference map have to be considered for quantification or the results of the paired t-test and the linear regression show enough accuracy to substitute the CT with the pseudoCT without further scaling.

4.2. Segmentation

4.2.1. Attenuation correction with DIXON

The AC DIXON is segmented from fat and water MRI images with compartments for soft tissue, fat and air. The further statistical analyses should reveal the impact of the ignorance

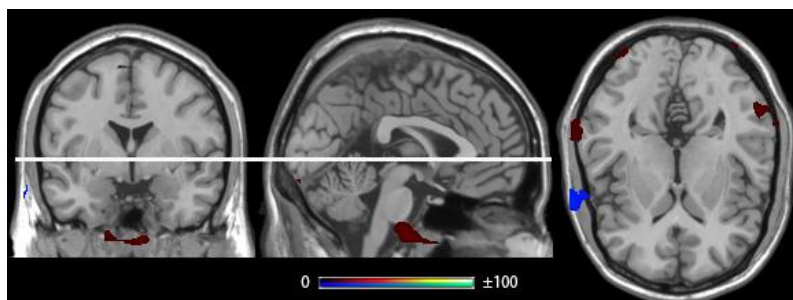


Figure 15: Statistical result of the paired t-test with $T > 8.59$, $p < 0.05$ FWE corrected, as threshold. The difference between $SUVs$ reconstructed with AC CT and $SUVs$ reconstructed with AC pseudoCT is significant only for two small lateral regions and outside of the brain.

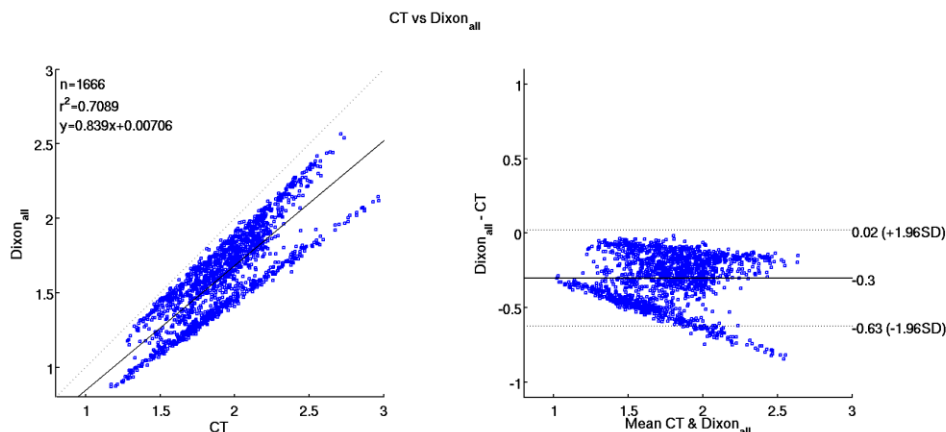


Figure 16: Correlation of ROIs between SUVs reconstructed with AC CT and AC DIXON_{all} (left). The scatter plot shows low correlation ($r^2 = 0.71$), a slope of 0.84 and an intercept close to zero. This indicates an underestimation of the reconstructed values with AC Dixon. The Bland-Altman plot (right) reveals a great deviation and underestimation from the center at -0.3, especially for higher binding regions. Furthermore, the patterns of the plotted data lead to the suggestion that the dataset should be split based on a feature for better correlation.

of bone. Because of the occurring tissue swaps this group was subdivided into DIXON_{all} (all subjects, no differentiation between correct segmented AC DIXON or tissue swap), DIXON_{ok} (only subjects with correctly segmented AC DIXON map) and DIXON_{ts} (only subjects with tissue swap in their AC DIXON map). This was also done because different performances were expected between DIXON_{ok} and DIXON_{ts}.

- **Attenuation correction with DIXON_{all}**

A linear regression based on the 98 ROIS was performed on the SUVs reconstructed with AC Dixon ($SUV_{DIXON_{all}}$) for all 17 subjects without distinction for DIXON_{ok} and DIXON_{ts}. Figure 16 shows the scatter plot (left) with a relatively low correlation of $r^2 = 0.7089$ and a regression line (slope = 0.839, intercept = 0.007) exposing a great underestimation of the $SUV_{DIXON_{all}}$ compared to the SUV_{CT} . The Bland-Altman plot on the right side of Figure 16 demonstrates a great variability (18%) from the center at -0.3 and an increasing underestimation of higher binding regions. Interestingly, both plots display a pattern where two different regression lines could be drawn with higher correlation suggesting two datasets of different behavior were wrongly merged.

The analysis on a voxel-wise basis can be seen in Figure 17. The difference map calculated from SUV_{CT} and $SUV_{DIXON_{all}}$ shows an increasing error from the center of the brain (approximately 10%) to the regions close to the bone (approximately 30%). This result suggests that bone might be important for correct quantification. Intriguingly, different ROIs can be distinguished by means of their increased circumscribed error, e.g. the thalamus. Errors above 40% are at the border of the skull and probably not in the brain, but spill-over effects from skull to cortex should be considered (see also statistical evaluation in Figure 16). The mean overall error was 16.86%.

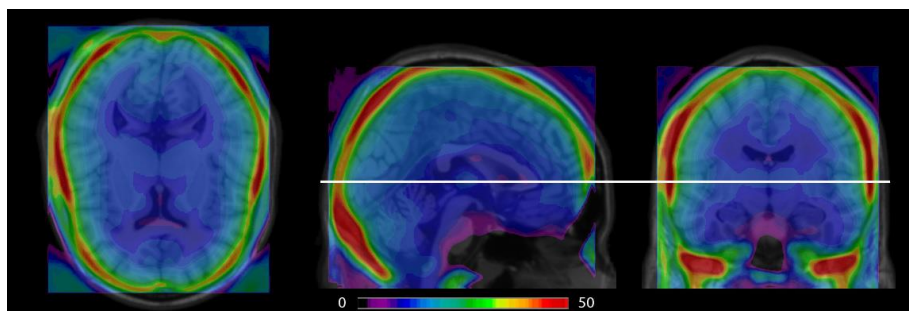


Figure 17: Voxel-wise difference map in percent of $SUVs$ reconstructed with AC CT and AC DIXON_{all}. The difference map shows an increasing error from the center of the brain (approximately 10%) to the regions close to bone tissue (approximately 30%). It should be remarked, brain regions can be distinguished by means of difference such as the thalamus. Although the difference map displays differences up to 50% these are in the border to the skull.

The statistical voxel-wise analysis was carried out with a paired t-test and revealed similar findings compared to the difference map. Although the differences between SUV_{CT} and $SUV_{DIXON_{all}}$ were significant close to bone, the errors close to the center of the brain were not significant with an FWE corrected threshold of $T > 8.47$ ($p < 0.05$) (see Figure 18) and the contrast SUV_{CT} greater than $SUV_{DIXON_{all}}$.

The results of the analyses of DIXON_{all} showed significant underestimations not only on a voxel-wise but also on an ROI basis leading to an erroneous quantification if not considered. The reason for this error is most probably the ignorance of bone which leads to a wrong attenuation and scatter profile.

The addressed patterns in the scatter and Bland-Altman plot of Figure 12 supported the hypothesis of different performances of DIXON_{ok} and DIXON_{ts}. Thus, these subgroups were investigated separately:

- **Attenuation correction with DIXON_{ok}**

The subgroup DIXON_{ok} consisted only of data reconstructed with correctly segmented AC Dixon. In the ROI-based scatter plot of SUV_{CT} and the $SUVs$ reconstructed with DIXON_{ok} ($SUV_{DIXON_{ok}}$) in Figure 19 (left) a higher correlation ($r^2 = 0.87$) and a regression line closer to the line of identity (slope = 0.90, intercept = -0.02) can be observed compared to Figure 16. The Bland-Altman plot (right) does not show increased underestimation in higher binding regions anymore but still a great fluctuation around the center at -0.22. If the center is

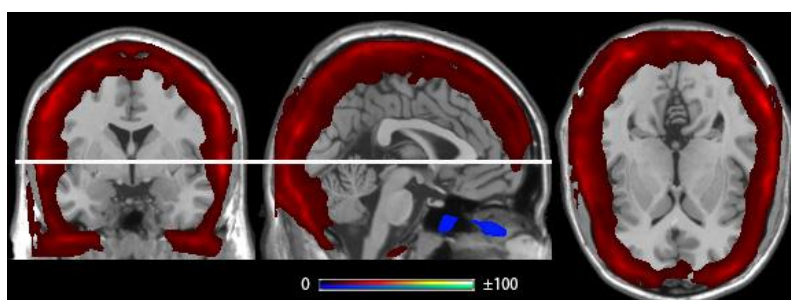


Figure 18: Statistical result of the paired t-test with $T > 8.47$, $p < 0.05$ FWE corrected, as threshold. The difference of $SUVs$ reconstructed with AC CT and $SUVs$ reconstructed with AC DIXON_{all} shows significant errors in the proximity of bone and therefore significant underestimations in this region.

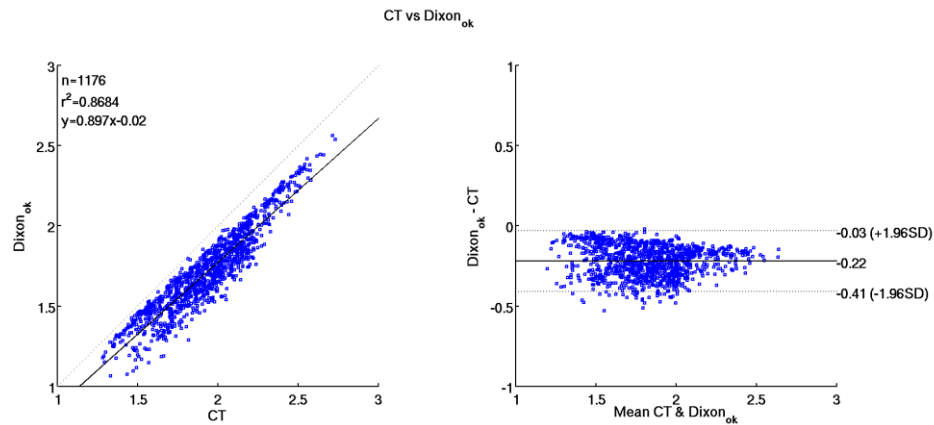


Figure 19: Correlation of ROIs between reconstruction AC CT and AC Dixon_{ok} (left). The scatter plot shows medium to high correlation ($r^2 = 0.87$). The regression line with a slope below 1 and an intercept close but below zero indicates continuous underestimations of the SUVs. The Bland-Altman plot shows a great deviation around the center of -0.22 and therefore an underestimation of the reconstructed values.

compared to the Bland-Altman plot of Figure 16 it is a bit closer to zero leading to the assumption of a smaller overall error.

The ROI based finding of a smaller overall error is supported by the voxel-wise difference map. Figure 20 shows a minor error close to the brain center (up to 5%, which was 10% for $SUV_{DIXON_{all}}$) and a greater error in the proximity to the bone (up to 20%, but 30% for $SUV_{DIXON_{all}}$). Despite the smaller overall error it is still possible to recognize brain regions by means of their increased circumscribed error, e.g. the thalamus. The mean error of the whole brain was 12.48%

The paired t-test of DIXON_{ok} delivers different results compared to DIXON_{all}. It shows significant differences across almost all voxels except for frontal regions and regions close to the bone, with $T > 11.57$, $p < 0.05$ FWE corrected (see Figure 21). The different results might arise from different sample size and the mutual analysis of DIXON_{ok} and DIXON_{ts} even though they perform differently.

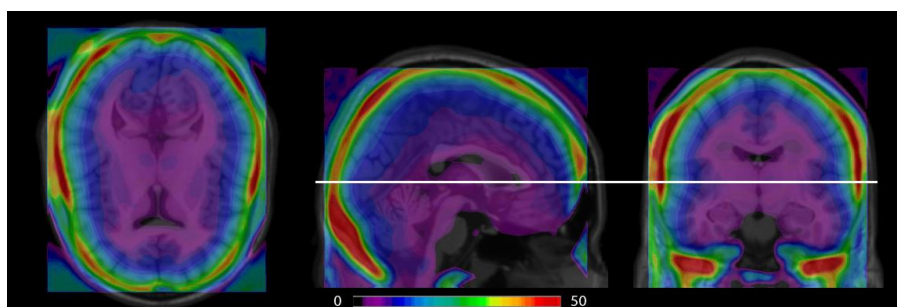


Figure 20: Voxel-wise difference map in percent of SUVs reconstructed with AC CT and AC DIXON_{ok}. The difference map shows an increasing error from the center of the brain (approximately 4%) to the regions close to bone tissue (approximately 20%). It should be remarked, brain regions can be distinguished by means of their difference such as the thalamus.

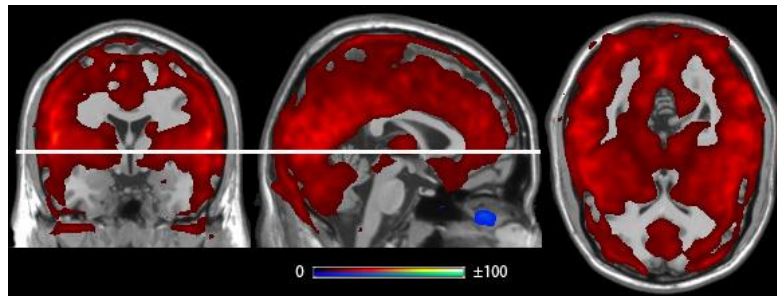


Figure 21: Statistical result of the paired t-test with $T > 11.57$, $p < 0.05$ FWE corrected, as threshold. The difference off reconstruction with AC CT and reconstruction AC Dixon_all shows significant errors across the whole brain except for small frontal regions.

- **Attenuation correction with DIXON_{ts}**

Because of the wrongly classified tissue in the AC DIXON with tissue swaps it is assumed that the reconstructions with AC DIXON_{ts} underestimate the real SUVs even more. A calculated regression line with a slope of 0.705 and an intercept of 0.0541 confirmed the assumption on an ROI basis (see Figure 22). Besides the underestimation the scatter plot shows a correlation ($r^2 = 0.99$) in the range of the pseudoCT ($r^2 = 0.99$) thus, higher than DIXON_{all} ($r^2 = 0.71$) and DIXON_{ok} ($r^2 = 0.87$) which suggests a linear scaling is possible to compensate the underestimations. The Bland-Altman plot (right) shows approximately the same variation around the center as DIXON_{ok}. However, the center can be found at -0.51 which is far below DIXON_{ok} (-0.22) indicating a higher underestimation of the SUV. Interestingly, a pattern can be seen in the Bland-Altman plot which reveals a greater underestimation for regions with a higher uptake compared to low binding regions.

The assumption was also confirmed on a voxel-wise basis by a calculated difference map which showed a high error all over the brain (see Figure 23). Interestingly, the error did not increase from the center of the brain like for the other reconstructions with AC DIXON but

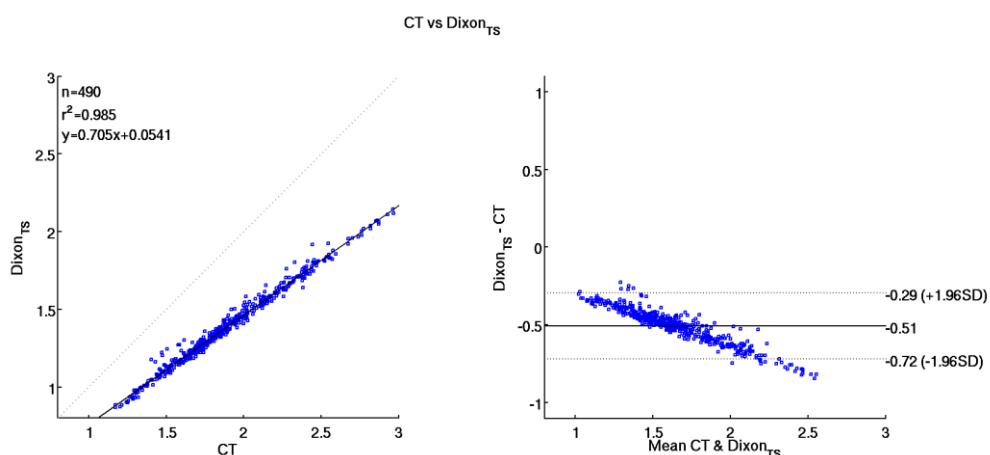


Figure 22: Correlation of ROIs between SUVs reconstructed with AC CT and AC Dixon_{ok} (left). The scatter plot shows higher correlation than the reconstructions with AC Dixon_{all} and AC Dixon_{ok}. Although the regression line indicates a great underestimation it should be possible to correct for the miscalculations with linear scaling due to the high correlation. The Bland-Altman plot (right) shows a large variation around the center of -0.51. The center far below 0 also demonstrates underestimation which increases with higher binding regions. Furthermore, the pattern found in the Bland-Altman plot indicates that ROIs with a lower uptake are less underestimated than regions with a high uptake.

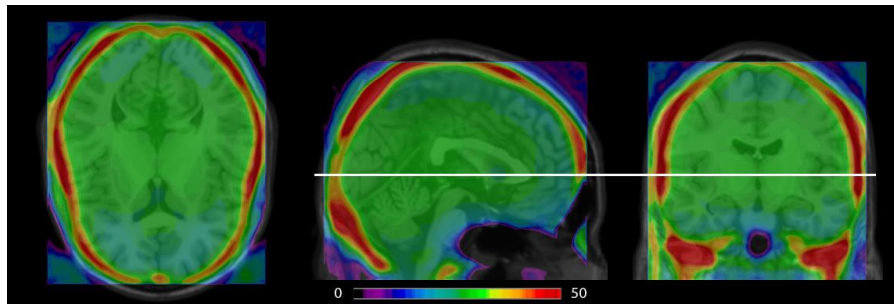


Figure 23: Voxel-wise difference image in percent for $SUVs$ reconstructed with AC CT and AC DIXON_{ts}. The difference map shows a higher error for the center of the brain (approximately 30%) than near bone (approximately 20%) and a higher error across the whole brain compared to DIXON_{all} and DIXON_{ok}.

the center showed a higher error (around 30%) than the voxels in the proximity to bone (around 20%) especially in the frontal region. The whole brain mean error was 27.36%

Although the significance of the errors was calculated with a paired t-test no significant voxels were found with FWE correction. The reason for this might be the small number of subjects ($n = 5$).

DIXON_{all} was split into the subgroups DIXON_{ok} and DIXON_{ts} because of the assumption of different performances encouraged by the two patterns that can be seen in Figure 16. Plotting again the scatter and Bland-Altman plot with the data of DIXON_{ok} in blue and the data of DIXON_{ts} in red shows perfect correspondence with the patterns found in Figure 16 (see Figure 24). This finding explains the patterns and reveals a different performance for AC DIXON_{ok} and AC DIXON_{ts} which has to be taken into account for quantification.

4.2.2. Attenuation correction with UTE

The AC UTE segments soft-tissue, air and also bone tissue which is different to AC DIXON. Thus, it is expected it underestimates the $SUVs$ of the reconstructions (SUV_{UTE}) to a lesser

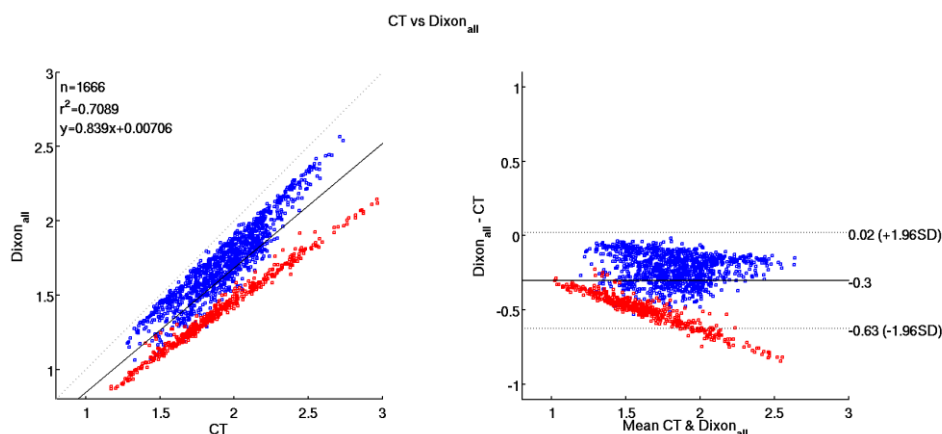


Figure 24: Correlation of ROIs between $SUVs$ reconstructed with AC CT and AC DIXON_{all}. It is the same figure as Figure 16 except for the colors, data of DIXON_{ok} in blue and data of DIXON_{ts} in red. The plots explain the different patterns and reveal that it is necessary to separate the analysis of DIXON_{ok} and DIXON_{ts} due to different performances.

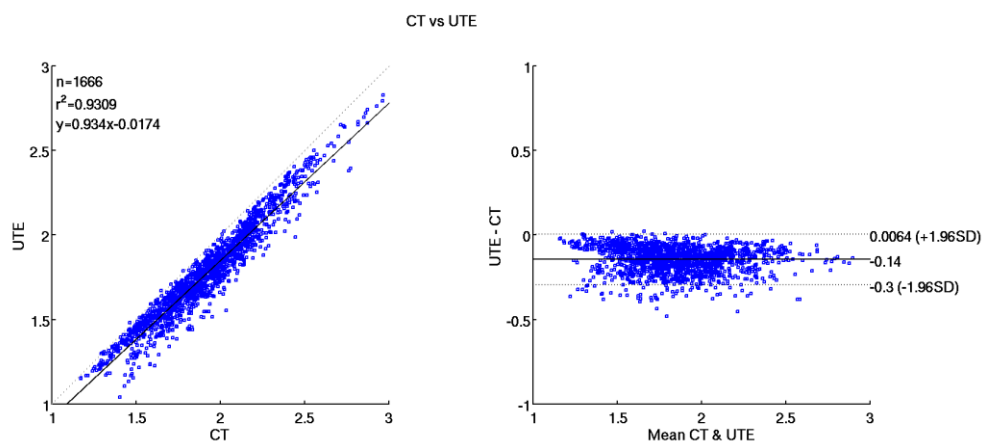


Figure 26: Correlation of ROIs between *SUVs* reconstructed with AC CT and AC UTE (left). The scatter plot shows high correlation and a regression line (slope = 0.93, intercept = -0.02) which indicates small underestimations. The Bland-Altman plot on the right shows medium variation around the center of -0.14 which means small underestimation should be expected.

extent than AC Dixon and might perform as good as the AC pseudoCT. In the scatter plot the data of the 98 ROIs show a high correlation of $r^2 = 0.93$ which is almost in the range of the pseudoCT ($r^2 = 0.99$) and a regression line near the line of identity (slope = 0.93, intercept = -0.02) which suggests small underestimations in ROI-based quantification (see Figure 26, left). The Bland-Altman plot on the right displays medium variation around the center at -0.14. The center below 0 is also an indication for underestimation but to a smaller extent compared to $DIXON_{all/ok/ts}$.

The underestimations found in the ROI-based analysis are also found in the voxel-wise difference map (see Figure 25). It can be seen that the center of the brain is lesser underestimated (around 5%) than the areas close to the skull (around 15%). However, the error is much smaller than the one of AC DIXON (see Figure 17) especially in the region of bone tissue. Interestingly, the brain stem displays a higher inaccuracy (20%) for the AC UTE than the AC DIXON which might be important for certain scientific questions. The mean difference across the whole brain was 7.85%.

The paired t-test shows significant differences for the contrast SUV_{CT} great than SUV_{UTE} with a threshold of $T > 8.55$, $p < 0.05$ FWE corrected, in accordance with the difference map (see Figure 27). The differences can therefore be found all over the brain except for caudal and

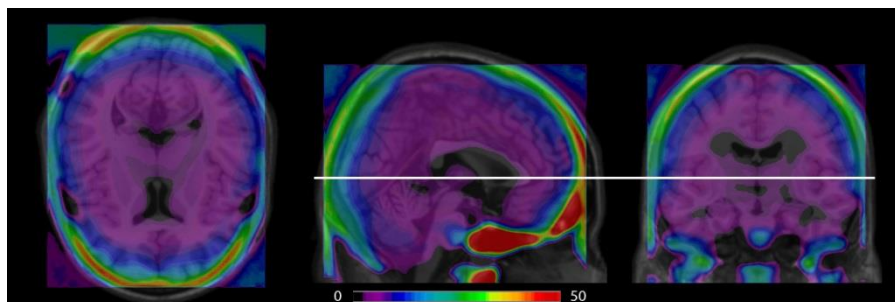


Figure 25: Voxel-wise difference map in percent for reconstruction with AC CT and AC UTE. The difference map shows a smaller error for the center of the brain (approximately 5%) than near bone (approximately 15%). A smaller overall error is in correspondence with the scatter and Bland-Altman plot. It should be remarked, brain regions can be distinguished by means of their difference such as the putamen.

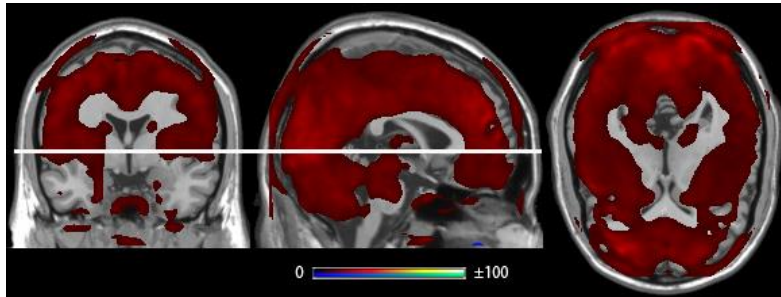


Figure 27: Statistical result of the paired the t-test with $T > 8.55$, $p < 0.05$ FWE corrected, as threshold. The difference of reconstruction with AC CT and reconstruction with AC pseudoCT shows significant errors across the whole brain except for caudal and frontal regions and the cerebellum.

frontal regions and the cerebellum. However, it is notable that the great errors found in the difference map seem to be insignificant.

In comparison to the previous results the AC UTE performs worse than the AC pseudoCT but better than the AC DIXON. The reason for this might be the attempt to segment bone. Although the skull is not always segmented accurately in this AC approach, especially in the occipital region, the importance of a bone segment for correct attenuation and scatter correction could be demonstrated.

4.3. Attenuation correction with transmission

The AC TX is generated by rotating rod sources, producing an attenuation profile. Due to a smaller field of view in the GE PET Advance scanner missing AC information was substituted with information from the AC Dixon. The attenuation profile shows a poor counting statistic but contains real LACs for photons with 511keV for all tissues which different compared to the segmentation approaches. Therefore, it is expected that it performs as good as the AC CT.

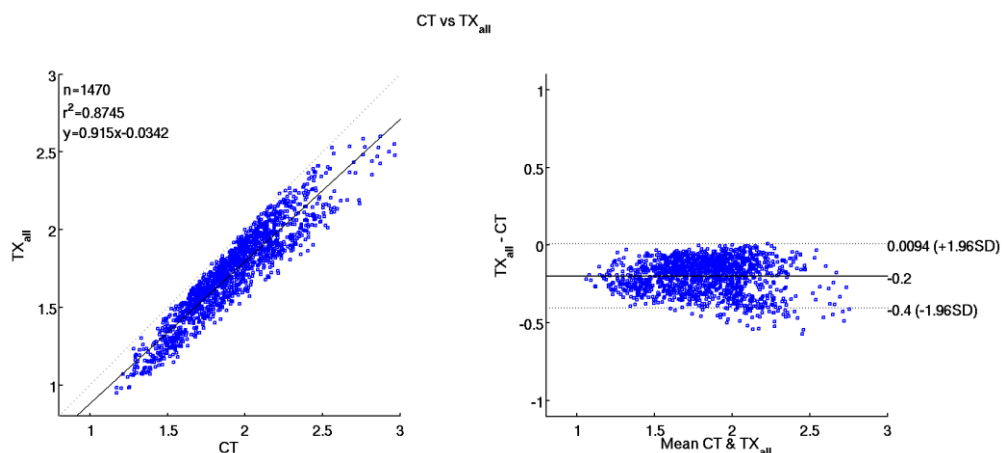


Figure 28: Correlation of ROIs between SUVs reconstructed with AC CT and AC TX_{all} (left). The scatter plot shows medium correlation and a regression line with slope = 0.92 and intercept = -0.03 showing moderate underestimations. The Bland-Altman plot on the right shows a similar variation around the center at -0.14 as AC UTE which confirms that underestimation should be expected.

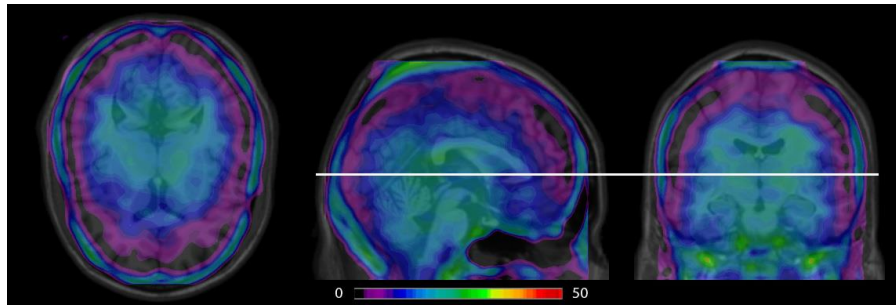


Figure 29: Voxel-wise difference map in percent for reconstruction with AC CT and AC TX_{all}. The difference map shows a smaller error at the proximity to bone tissue (approximately 5%) and a higher error close to the center of the brain (approximately 25%) which is the opposite to what was already shown for DIXON and UTE.

Because of the substitution with information from the AC DIXON in areas without TX information an incorporation of AC DIXON with a tissue swap can happen especially in the neck region. If this incorporation has an influence on the performance of the AC TX was investigated by splitting the data reconstructed with AC TX into TX including all subjects which underwent a GE-PET scan (TX_{all}), TX with subjects with correctly segmented AC DIXON (TX_{ok}) and TX with subjects with tissue swaps in their DIXON AC map (TX_{ts}):

- **Attenuation correction with transmission_{all}**

Although the AC TX should theoretically perform as good as the AC CT due to its method of acquisition, the results do not support the theory. A ROI-based linear regression with SUV_{CT} and the SUV s reconstructed with AC TX_{all} ($SUV_{TX_{all}}$) demonstrates an underestimation of the $SUV_{TX_{all}}$ with a slope of 0.92 and an intercept of -0.03 (see Figure 28:, left) approximately in the same range as the AC UTE. The correlation of this data has an r^2 of 0.87, which is in comparison to the previous results only better than DIXON_{all} and DIXON_{ok}. Also the Bland-Altman plot shows similarities to AC UTE with a slightly higher variation and underestimation of the SUV s compared to UTE. Furthermore, while the AC UTE had the center at -0.14 the AC TX has it at -0.2 (see Figure 29, right) showing underestimations to a higher degree. However, no pattern similar to DIXON_{all} can be found.

A bigger variation to the other results can be found in the voxel-wise calculated difference map. The map reveals a good estimation of the skull in the AC TX by showing the smallest error near bone (approximately 5%) while the error into the direction of the brain center increases to up to 25%.

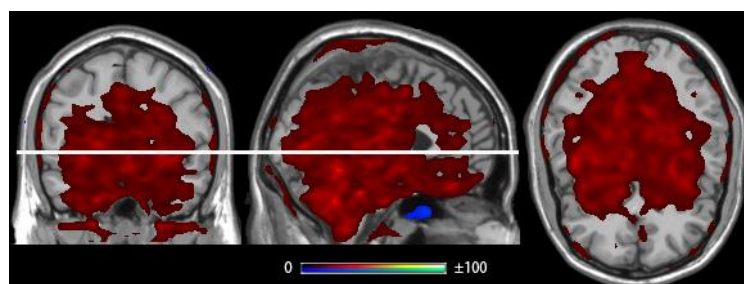


Figure 30: Statistical result of the paired t-test with $T > 9.53$, $p < 0.05$ FWE corrected, as threshold. The difference between AC CT and AC TX_{all} was significant across the whole brain except for regions close to the bone.

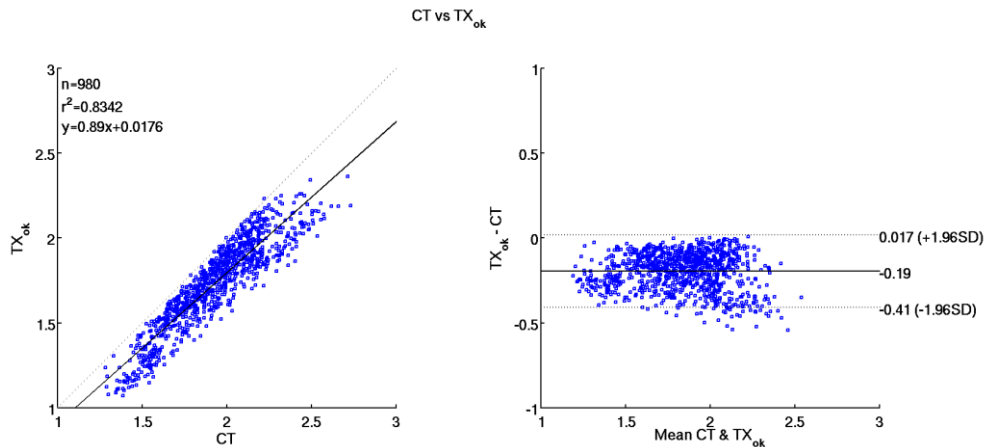


Figure 31: Correlation of ROIs between *SUVs* reconstructed with AC CT and AC TX_{ok} (left). The scatter plot shows medium correlation ($r^2 = 0.83$) and a regression line with slope of 0.89 and of intercept = 0.02 leading to moderate underestimations. The Bland-Altman plot on the right shows variation of 12% around the center at -0.19. Both results are similar to the ones shown for TX_{all}.

Furthermore, the paired t-test indicates that the smaller errors found in the difference map in the closest proximity to the skull are not significant with the contrast SUV_{CT} greater than $SUV_{TX_{all}}$ and a threshold of $T > 9.53$, $p < 0.05$ FWE corrected but only the variations closer to the center of the brain. A few voxels on the outside of the brain are also significant but can be neglected.

The results of the performance of the AC TX_{all} show a good estimation of the *SUVs* in the area of the skull. The reason for this might be the technique of the acquisition of the TX which seemingly reflects the LACs of the skull correctly without the necessity for further scaling. The underestimation of the soft tissue in the proximity to the center of the brain might arise from the poor counting statistic and thus from regions with too few annihilation events.

- **Attenuation correction with transmission_{ok}**

A ROI-based correlation of *SUVs* reconstructed with AC TX, only with correctly segmented AC Dixon ($SUV_{TX_{ok}}$), and SUV_{CT} shows an $r^2 = 0.83$ which is a bit smaller than for AC TX_{all} (see Figure 31). Also the regression line (slope = 0.89, intercept = 0.02) of AC TX_{ok} is a bit further away from the line of the identity compared to the regression line of TX_{all}. This would lead to a slightly higher error when scaling the data. The Bland-Altman plot of TX_{ok} (right) is almost identical to TX_{all} with the center at -0.19 and the same variation indicating an underestimation of a similar magnitude.

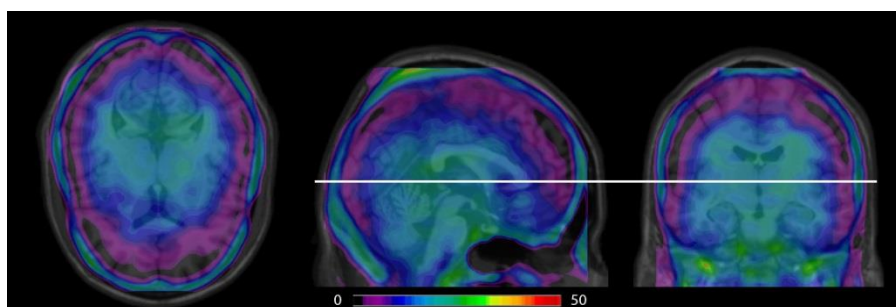


Figure 32: Voxel-wise difference map in percent for reconstruction with AC CT and AC TX_{ok}. The resulting difference map shows almost the exact same error as for TX_{all}: The error near bone tissue is around 5% and near the center 25%.

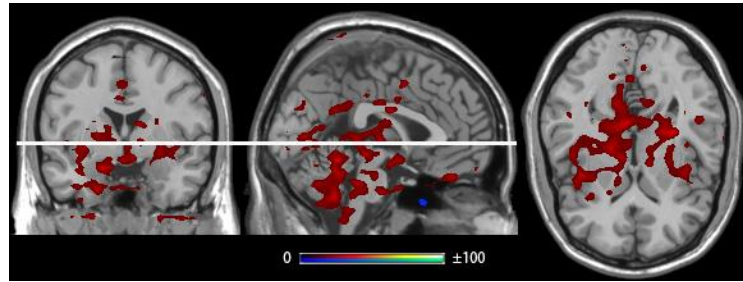


Figure 33: Statistical result of the paired t-test with $T > 14.32$, $p < 0.05$ FWE corrected, as threshold. The difference of reconstruction with AC CT and reconstruction with AC TX_{ok} shows significant errors comparable to TX_{all} but thinned out, probably due to the smaller sample size.

Although there are small differences in the scatter and Bland-Altman plot between TX_{ok} and TX_{all} , it is impossible to visually find these differences in the voxel-wise calculated difference map anymore suggesting that the differences can be neglected (see Figure 32).

Because of the equality of the difference maps of TX_{all} and TX_{ok} the same equality was expected for the result of the paired t-test. However, the paired t-test showed less significant voxels with a threshold of $T > 14.32$, $p < 0.05$ FWE corrected, across the whole brain which is probably based on the smaller sample size $n = 10$ (see Figure 33).

The whole investigation of the separately treated data reconstructed with AC TX_{ok} showed only minor difference between TX_{all} and TX_{ok} leading to the assumption that it does not matter if the unknown area of the neck is substituted with a correct or tissue swapped AC DIXON map.

- Attenuation correction with transmission_{ts}

This last suggestion is supported by the ROI and voxel-wise analyses of the data reconstructed with AC TX with incorporated AC DIXON_{ts}. A correlation of the SUV_{CT} and the $SUVs$ reconstructed with AC TX_{ts} ($SUV_{TX_{ts}}$) shows a similar but higher r^2 of 0.92 and a regression line almost in the same distance to the line of identity compared to TX_{all} ,

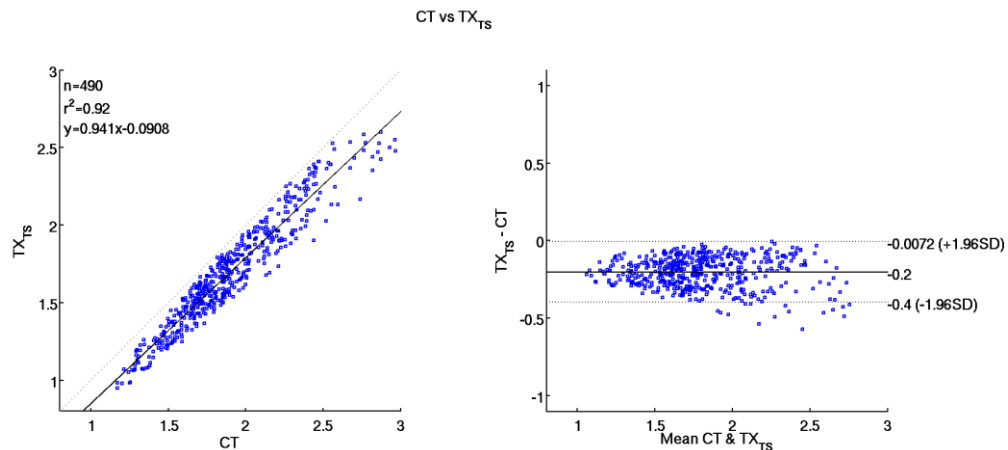


Figure 34: Correlation of ROIs between $SUVs$ reconstructed with AC CT and AC TX_{ts} (left). The scatter plot shows high correlation ($r^2 = 0.92$) and a regression line with a slope of 0.94 and an intercept of -0.09 which is in the range of TX_{ok} and TX_{all} . Also the Bland-Altman plot (left) is in the same scale as TX_{ok} and TX_{all} in terms of variation and the center at -0.2.

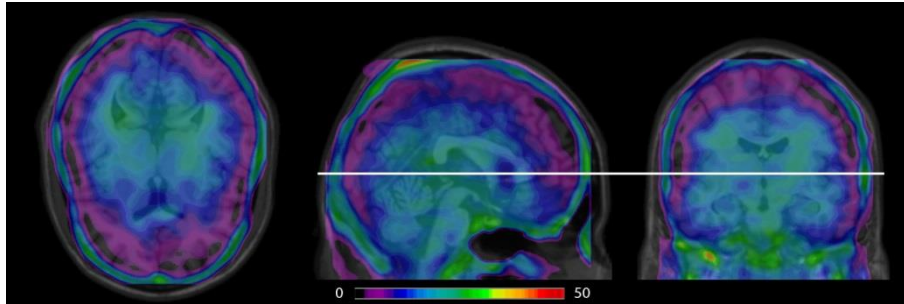


Figure 35: Voxel-wise difference map in percent for reconstruction with AC CT and AC TX_{ts}. The resulting difference map shows almost the exact same error as for TX_{all} and TX_{ok} : The error near bone tissue is around 5% and in this case an error near the center of the brain of around 30%

indicating an underestimation in the same scale(see Figure 34). Also the Bland-Altman plot (right) shows the exact same center at -0.2 and almost the same variation.

Additionally, the visual analysis of the voxel-wise difference map also shows almost no difference compared to TX_{all} and TX_{ok} (see Figure 35) except for a slightly higher error in the center of the brain of around 30%. Furthermore, a paired t-test was carried out but did not show significant voxels with FWE correction and $p < 0.05$, probably due to the small sample size of $n=5$.

Finally, from these results it can be concluded there is no difference in the reconstructed data regardless of the usage of correctly segmented AC DIXON or the AC DIXON with tissue swap. The whole data is plotted again, this time in different colors. The subjects without a DIXON tissue swap in the AC TX were plotted in blue, subjects with a DIXON tissue swap were plotted in red. In Figure 36 it can be seen that differently to AC Dixon, analyzing the data as AC TX_{all} is accurate because both data sets show the same behavior. Thus, it can be concluded that only the LACs of the skull and soft tissue of the head are important for AC but not the LACs of the neck region.

A summary of all presented values and AC approaches can be found in Table 1 and Figure

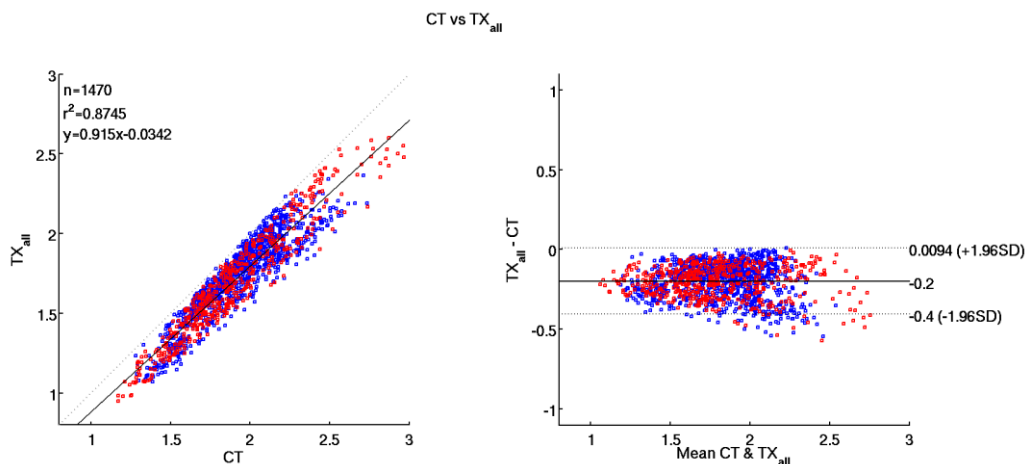


Figure 36: Correlation of ROIs between SUVs reconstructed with AC CT and AC TX_{all}. It is the same figure as Figure 28 except for the colors, data of TX_{ok} in blue and data of TX_{ts} in red. The plots do not show different patterns such as DIXON_{all} leading to the assumption that the LACs of the neck region do not influence the AC in the brain.

37.

Table 1: Slope, intercept and r^2 values for all AC approaches compared to AC CT

	Slope	Intercept	r^2
pseudoCT	1.02	-0.05	0.99
DIXON _{all}	0.84	0.01	0.70
DIXON _{ok}	0.90	-0.02	0.87
DIXON _{ts}	0.71	0.05	0.99
UTE	0.93	-0.02	0.93
TX _{all}	0.92	0.03	0.87
TX _{ok}	0.89	0.02	0.83
TX _{ts}	0.92	-0.09	0.92

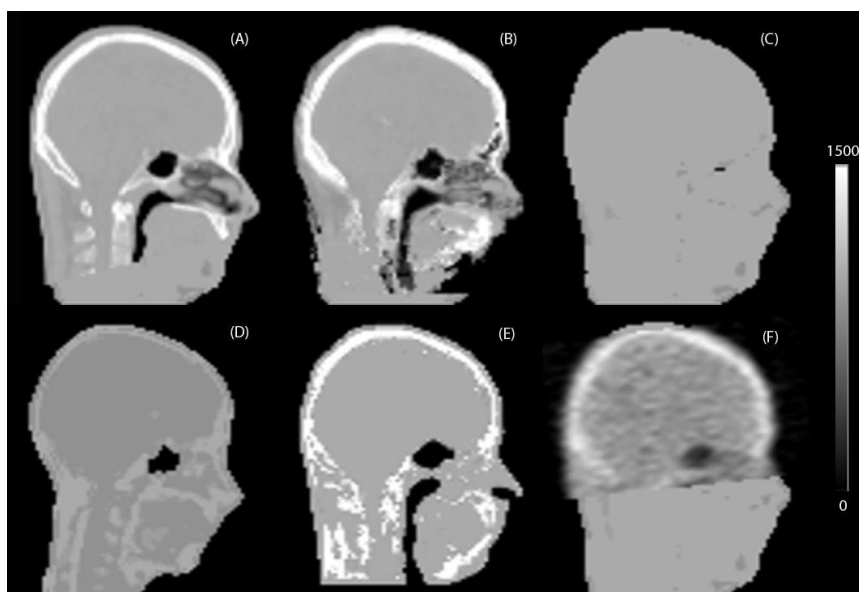


Figure 37: Summary of all presented AC maps: (A) CT, (B) pseudoCT, (C) correct DIXON, (D) DIXON tissue swap, (E) UTE, (F) Transmission with DIXON in neck region.

5. Discussion

The necessity of AC for correct PET images is undoubted by the scientific community and proven by several authors e.g. (Kinahan et al. 1998; Huang et al. 1979; Bailey 1998). Thus, the aim of this work was not to create another proof of the importance of the AC but to examine the possibility to substitute the gold standard AC method CT with an alternative approach. The reason for this is the mentioned unfeasibility to record an additional low-dose CT for the clinical routine because of the increased logistic and computational demands as well as lack of trained staff and time. Furthermore, the low-dose CT exposes the subjects to further radiation which should be kept at a minimum. Therefore, different AC approaches based on different techniques were compared to the AC CT to evaluate their performances, assets and drawbacks.

- **Attenuation correction with pseudoCT**

The AC pseudoCT is a mean image of several CTs from an atlas database with CT-MR pairs and performed best in terms of reproducibility and bias compared to the other AC approaches. The inventors of this approach also used the AC CT as gold standard and compared their method against it (Burgos et al. 2014). The results found in this work are similar to the ones found by Burgos et al. (2014), although they used different measurements for comparison. The authors calculated an r^2 value of 0.988 on a voxel-wise basis and the regression coefficients slope and intercept equal to 1.009 and -83 respectively, on normalized data. These values are almost identical to the ROI-based results found in this work except for the intercept, which might be based on different scaling. However, their joint histogram on a voxel-wise basis also looks similar to the scatter plot of the ROIs in Figure 13 (left). Additionally, the relative mean error (rME) of $-0.17\% \pm 2.11$ calculated by Burgos et al. is in accordance with the voxel-wise mean values calculated from the difference map between SUV_{CT} and $SUV_{pseudoCT}$ ($2.47\% \pm 1.86$) estimated in the present work. The negative rME shows that the inventors found a slight mean overestimation of the values reconstructed with their pseudoCT approach which could not be found in the used data set. However, the small errors and great similarities of the results compared to (Burgos et al. 2014) emphasize the good accuracy of this AC approach and support the validity of the outcome of the present work.

It is assumed that the great accuracy is based on the similarity to the CT and its LACs. Since the attenuation correction is based on the integral of the LACs along a line of response (LOR) the LACs are defining the accuracy of the approach to a greater extent. The inaccuracy of the frontal region probably arises from the individual differences of the frontal sinuses which are hard to depict from a mean image.

Additionally to the good accuracy, the method is easy to apply due to the website provided by the UCL. A target T1- or T2-weighted MRI has to be uploaded, albeit in NifTI and not in

standard DICOM format generated by the PET/MR scanner. Such a target MRI is recorded not only in research studies for preprocessing purposes but is also part of the standard protocol in the clinical routine, where it is used for fusion with the PET image for anatomical localization due to its better spatial resolution. Therefore, no additional scan time is needed for clinical routine.

However, drawbacks are the necessity for further processing of the target MRI before it can be used as AC (see chapter 3.3.2) and the additional computation time of the pseudoCT of two to three hours. Another limitation is the necessity of a morphologically healthy subject, since the atlas database consists only of such subjects. Using the pseudoCT on a patient with a lesion or missing skull would lead to wrong AC because of an over- or underestimation of the LACs in these areas.

Therefore, the usage of the pseudoCT is unfeasible in the clinical routine. Differently, AC pseudoCT seems to be a good alternative for the low-dose CT for research studies because the correct absolute quantification plays a superior role compared to time. Because of the possible substitution of the CT it would be a major gain for the scientific community if the vendor implemented this AC approach making the preprocessing steps redundant, thus decreasing computational effort.

An improvement of this approach could be a distinct weighting of different head areas such as frontal or occipital regions instead of the same weight for the entire CT for the conversion to pseudoCT. However, this needs further evaluation.

- Attenuation correction with DIXON

The AC DIXON is calculated from in- and opposed-phase MR images and is then segmented according to the values of the voxel intensity into soft tissue, fat and air. The ROI-based scatter plot of $SUV_{DIXON_{all}}$ and SUV_{CT} showed a pattern which led to a distinction of the data into AC DIXON with correct segmentation ($DIXON_{ok}$) and AC DIXON with tissue swaps ($DIXON_{ts}$):

- Attenuation correction with $DIXON_{ok}$

The overall performance of this AC approach was rather poor compared to all other AC methods. The ROI-based scatter and Bland-Altman plot of $DIXON_{ok}$ showed an increased underestimation which was also found in the voxel-wise difference map. The error increased from the center of the brain from approximately 4% to around 20% in the proximity to the skull. In previous studies errors in the same range were found. Other groups reported errors occurring from underestimation of up to 20%, 14% and 14 – 16%, respectively in the area of bone tissue (Dickson et al. 2014; Samarín et al. 2012; Keereman et al. 2010). Also Ladefoged et al. (2015) showed a similar error of 5% at the center of the brain and 15% close to the skull.

Additionally, brain regions are also delineated by means of their error as found in the present work.

Besides the similar findings in previous works an estimated r^2 of 0.66 between values of DIXON_{ok} and CT was reported earlier which is not in agreement with the r^2 of 0.87 found in the present work (Ladefoged et al. 2015). The differences might arise from the different type of calculation. The authors used all voxels to calculate the r^2 while in this work the r^2 was estimated on the basis of the means of 98 ROIs.

Another disagreement with a previous work was found for the whole-brain bias. Koesters et al. (2016) report a voxel-wise whole brain underestimation of 6.4% between values reconstructed with DIXON_{ok} and CT. In the present work the bias was 12.48%. The great difference arises from different preprocessing steps of the CT data. The group removed the bed and neck holder of the CT by applying the AC DIXON as mask which falsifies the CT. The AC DIXON is too small in most cases and can have huge air gaps so if it is applied as a mask LACs of skull and soft tissue might be lost. The missing LACs then lead to an underestimation of the values reconstructed with the reference CT due to wrong AC and scatter correction. Therefore, the whole brain bias reported by the authors seems smaller while it is actually wrong because of an underestimation in their ground truth.

The overall underestimation occurs because of the missing bone segment. As already mentioned, the integral of the LACs along the LOR is used for attenuation correction. If the LACs are too low the attenuation is underestimated and therefore the reconstructed values.

- Attenuation correction with DIXON_{ts}

DIXON tissue swaps originate from off-resonance effects which arise from B_0 field inhomogeneity (Ladefoged et al. 2014). The occurrence of a DIXON tissue swap was rather common for the subjects used in the present work (28%). Another group investigated the brain AC DIXON of 283 subjects and reported a much smaller number of tissue swaps (8.1%) (Ladefoged et al. 2014). A reason for this might be found in the different cohorts. The reported mean age was 71 ± 14 years while the mean age of the subjects in the present work was much lower with 25 ± 4 years. A hypothesis is that the lower body mass index of younger people leads to the tissue swap. The real cause for an increased number of tissue swaps in younger people has to be further evaluated.

The ROI-based scatter and Bland-Altman plot of $SUV_{DIXONts}$ showed a great underestimation as compared to SUV_{CT} which could also be seen in the voxel-wise difference map. Furthermore, the group of Ladefoged et al. (2014) stated that the difference between the uptake values of correctly segmented DIXON and DIXON with tissue swap can be up to 35%. This error can also be seen when Figure 20 and Figure 23 are compared.

Comparing these figures it can also be seen that the difference to the SUV_{CT} is smaller near the skull region compared to the center in Figure 23. However, the r^2 of 0.99 indicates a great correlation of the data. Therefore, it would be possible to scale the data (slope = 0.71, intercept = 0.05) linearly to the range of the ROI values reconstructed with AC CT. It should be noted that the sample size was rather small and therefore this scaling may be only valid for ROIs.

The reason for the great correlation might be a similar distribution of the LACs compared to AC CT. This similarity can be seen in Figure 9B where soft-tissue is segmented in the area of bone and the rest as fat or air leading to a CT-like image. With this finding it can be hypothesized that the values of the LACs are less important than their distribution, as long as three segments can be distinguished. The hypothesis is supported by (Andersen et al. 2014), Figure 20 and Figure 23. The other group showed a great spatial error when bone is ignored with higher errors near the skull (Andersen et al. 2014). The reason for this is that areas close to the skull have to pass more bone tissue with high LACs before reaching the detector and are therefore more prone to attenuation and scatter. This is important because the integral of the LACs along the LOR are used for correction. In Figure 20 it can be seen that no LACs for bone were estimated because the highest difference can be found close to the skull. Differently, in Figure 23 a smaller error near the skull is seen indicating higher LACs than in the center of the brain were assigned in this area.

An asset of the AC DIXON is that it is already implemented by the vendor so no further processing is necessary. It is also quite fast and routinely recorded. Therefore, it would be a good alternative for the CT.

Unfortunately, the drawbacks predominate. The variation in the performance of $DIXON_{ok}$ and $DIXON_{ts}$ is an issue for research studies but also for clinical routine. It is common that a subject or patient undergoes a measurement and after some time a follow up measurement is performed. If for one measurement a DIXON tissue swap happens and not for the other one it is impossible to compare these measurements due to the shown different performances. To overcome this issue the vendor suggests to inspect the AC DIXON during the measurement and to repeat the sequence in case of the occurrence of issues. Ladefoged et al. (2014) investigated this suggestion and found that DIXON AC maps are reproducible. Out of 17 subjects tissue swaps were either found in both of the scans or none of them except for two subjects. These two had one correct AC DIXON and one with a tissue inversion. It seems the recommendation of the vendor is not valid for tissue swaps.

Furthermore, tissue swaps do not necessarily have to happen for the whole body part examined. A partial DIXON tissue swap was found for two subjects in the head (Ladefoged et al. 2014). Additionally, in whole body examinations tissue swaps can also occur in only one of the legs.

Another drawback is the non-uniformly distributed difference compared to the AC CT. The difference in magnitude of the error between the regions near the skull and the center of the brain influences the values of large ROIs spanning from bone to the center. The mean ROI values are falsified because the correctness of the reconstructed uptake values depends on the location. This is important for patients with brain tumors. Imagine an ROI drawn on a big tumor spanning from the frontal lobe to a subcortical region and reconstruction with a correctly segmented DIXON AC map. The lower uptake values near the skull decrease the mean value of the ROI which might lead to a wrong classification of the tumor and to a wrong therapy.

Since the AC DIXON is commonly used for clinical routine due to the lack of an alternative it is important that physicians are aware of the fact that the values near the skull are too low when AC is carried out with AC DIXON.

For the sake of completeness truncation artifacts should be mentioned. Truncation artifacts of the arms only occur in whole-body examinations when the arms are placed beside the patient. The reason for this is the limited field of view of the MRI compared to the one of the PET. With the incorrect depiction of the arms no or insufficient AC is performed in these areas but also in the torso. The reason is that the arms attenuate the photons as well but cannot be taken into account because they are missing in the AC map. The result is an underestimation of the uptake values up to 50% (Keller et al. 2013; Delso et al. 2010).

For research studies the AC DIXON approach is not applicable. Besides the underestimation and therefore the bias in absolute quantification, the unreliability of the DIXON algorithm in terms of tissue swaps makes it impossible to use it as an alternative for the CT. If a tissue swap occurred for a subject it would have to be excluded from the group statistic due to the different performances of DIXON_{ok} and DIXON_{ts} which is unbearable in terms of radiation burden to the subject and the entire scanning effort.

Nonetheless, the errors of 50% found in the proximity to bone might also spill over to nearby cortical brain areas. This may lead to a similar problem as with some [¹⁸F]-labeled radioligands which show a great amount of defluorination and hence uptake of [¹⁸F]fluoride in the bone. Due to the limited spatial resolution of PET imaging, the consequence is a spill-over effect of radioactivity to the adjacent cortex (Pike 2009). In this context, the high error found in the proximity of the bone region seems to spill-over also to the cortex, which in turn may lead to inaccurate quantification for areas near the bone.

Another drawback is the susceptibility of the AC DIXON to other artifacts: In this work it could be observed that the AC DIXON is smaller than the AC CT in most cases. The smaller size leads to missing LACs which enhances the effect of underestimation. In addition, the AC DIXON ignores air cavities such as the frontal sinus and fills it with soft tissue, also leading to wrong AC.

An alternative approach for the CT could be recording the DIXON always with a tissue swap by adapting the algorithm. The strong correlation obtained here suggests the possibility of scaling underestimated uptake values to correct uptake values at least for ROIs. To proof this hypothesis more data has to be gathered and evaluated.

- Attenuation correction with Bone demonstrator

A new AC prototype based on the AC DIXON was invented by Siemens Healthcare and first reported in 2015. The images produced by the DIXON VIBE sequence are used to incorporate bone as another segment. For the insertion of the skull an aligned MR-bone image pair is registered to the individual MR. Thereafter, the registered bone model is incorporated into the AC DIXON with continuous LACs valid for 511keV (Paulus et al. 2015). Although the approach seems similar to the pseudoCT the bone demonstrator incorporates fixed bone values into the AC DIXON whereas the pseudoCT consists of a mean CT image.

An improvement of the uptake values is reported in the brain area from an underestimation of 6.7% with AC DIXON to an overestimation of 2.7% with the prototype (Koesters et al. 2016). Therefore, they claim that the approach is better than the atlas-based approach pseudoCT invented by the group of (Burgos et al. 2014). As already mentioned the reference was falsified because the neck holder was cropped by applying the AC DIXON as mask (Koesters et al. 2016). Thus, their results have to be evaluated with great caution. However an improvement as compared to DIXON is probable due to the integration of bone LACs.

- Attenuation correction with UTE

The AC UTE originates from a dual gradient echo sequence. An R2 map which describes the fast transversal relaxation rate is calculated and segmented into bone tissue, soft tissue and air. The segmentation of bone leads to a smaller underestimation of the *SUVs* on a ROI and voxel-wise basis and also to a higher r^2 compared to AC DIXON. The ROI based slope and intercept are in better accordance with the line of identity than the parameters of $DIXON_{all/ok/ts}$. Also the voxel-wise error near the skull is smaller than with AC DIXON. This was also found in a previous work (Dickson et al. 2014). The authors report an error near the skull of 15% which is in the same range of the error found in this work (20%). Similarly, underestimations of 20 – 40% and 20% near bone tissue were found in earlier works (Keereman et al. 2010; Berker et al. 2012). However, the mean overall difference found in this work was 7.9% which is a bit less than $DIXON_{ok}$ and similar to another reported error of 6.9% (Ladefoged et al. 2015).

Although, the performance of AC UTE is better than AC DIXON it still shows a great underestimation compared to AC CT. The miscalculation probably originates from

underestimated LACs in the segmentation process. Since one of the issues of MRI signal is that the voxel intensity cannot be directly translated to Hounsfield units a fixed LAC has to be chosen for the whole skull. Compared to the AC CT this is inappropriate because in dense bone very high LACs can occur. As described previously, the attenuation of a photon is the integral of all LACs along a LOR. If the sum of the LACs is too small the same phenomenon as for DIXON_{ok} happens, the uptake is underestimated. However, due to the bone segment and the higher LACs the underestimation is decreased especially in the area of bone.

Unfortunately, the AC UTE is also prone to artifacts. The B_0 field inhomogeneity leads to wrongly segmented areas which can be seen in Figure 10 (Dickson et al. 2014). In the occipital region voxels were incorrectly assigned to the bone segment while bone was wrongly classified as soft tissue in the cranial region. This commutation can be seen all over the head and leads to discontinuities in the skull (Ladefoged et al. 2015). Additionally, in the frontal regions the ignorance of air in the frontal sinus can be observed. Different to the AC DIXON this area was assigned to bone tissue, leading to a wrong AC.

Although the AC UTE performs better than AC DIXON it is still neither useful for clinical routine nor for research studies. In the clinical routine the AC UTE is not part of the standard protocol which leads to additional scan time. For research the AC UTE is too inaccurate since the error is not uniformly distributed but shows a higher error close to the skull which makes the error not scalable.

Since the main idea of deriving an AC map from the R2 map seems promising, the approach was further improved as described in the following section (Ladefoged et al. 2015).

- Attenuation correction with “RESOLUTE”

The authors proposed a new AC method for the brain which should be more accurate than the AC UTE and also applicable for the clinical routine, named RESOLUTE (“Region specific optimization of continuous linear attenuation coefficient based on UTE”). Therefore, they also calculated an R2 map with the same equation used previously (Keereman et al. 2010). However, by thresholding the intensity they created different segments compared to AC UTE, namely bone, brain, soft tissue, cerebral spinal fluid (CSF) and air. In areas where a mixture of tissue and air is expected masks were applied with different values for thresholding such as in the area of the frontal sinus, the nasal septa, ethmoidal sinuses, the skull base and the mastoid process. The reason for this is voxel intensity inaccuracy arising from the mentioned mixture of tissue and air.

The similarity to the AC CT results in a better performance than the AC UTE. While the authors reported an overall underestimation of 6.9% for AC UTE they could reduce this error to 0.1% with their method. The voxel-wise difference map between the PET uptake reconstructed with CT and RESOLUTE, respectively, only shows small overestimations in

cranial regions close to the bone (up to 3%) and underestimations of up to 3% in occipital regions close to the bone and the cerebellum. Furthermore, the r^2 value could be improved from 0.78 to 0.92 on a voxel-wise basis.

Ladefoged et al. (2015) could demonstrate that their UTE-based approach AC RESOLUTE performs evidently better than AC DIXON and AC UTE. The good results suggest that a substitution of the CT is possible. The small error across the whole brain and also in the cerebellum makes it applicable for absolute quantification in research studies. The accuracy of the uptake in the cerebellum is particularly important because it is often used as reference in reference tissue models.

A drawback is the complicate processing of the UTE sequences to achieve the accurate AC RESOLUTE. Although the authors state that the clinical feasibility is still under investigation it is presumed that it will not be used in routine unless it is implemented by the vendor due to time, personal and technical knowledge issues.

- Attenuation correction with TX

Previously to this work we hypothesized that the AC TX performs in the same range as the CT. The reason for this assumption was the method of the acquisition of this AC approach. Rod sources are rotating around a subject producing events from annihilation. The emitted photons pass through the body. By means of their scatter and attenuation an individual attenuation profile is generated valid for 511keV which is the same energy as the photons produced from the annihilation from tracer positron decays.

However, the results in this work revealed that the hypothesis has to be discarded. The slope and intercept of the ROI-based regression line are in the range of the UTE while the r^2 is smaller and rather in the range of DIXON_{ok}. Therefore, this method underestimates the *SUV* values as well although in a different location. While the AC approaches DIXON and UTE underestimated the *SUVs* in the region of bone to a greater extent than in the center the TX performs vice versa. This suggests that the TX method depicts bone correctly in the AC map. Differently, the soft tissue seems to be assigned with too low LACs, which is potentially attributable to worse SNR of TX as compared to CT.

The calculated overall error found in this work was 10.67%, 10.39% and 11.23% for TX_{all}, TX_{ok} and TX_{ts}, respectively. The similarity of the overall error, the r^2 , slope and intercept of all three groups suggests that it does not matter if the neck region is depicted with LACs of fat or soft tissue. The slight variations may arise from the small sample size of TX_{ts}. However, for the reconstruction algorithm it is important that the neck region is depicted with anything different than air. In a single subject analysis decreased *SUV* values were found if the neck region had LACs of air (data not shown). The reason for this is that the neck is needed for appropriate scatter correction.

However the observed differences in this work only partly match with the results of the literature. Nakamoto et al. (2002) report an underestimation of around 5% in the cerebellum and the temporal lobe. In the present work an error of approximately 5% and 12% was reported for these regions. A possible reason for the difference is the varying underlying data and the different length of the transmission scan. The AC CT was compared to the AC TX with data acquired on a PET/CT (Nakamoto et al. 2002). The different detector sensitivity of a PET/MR and PET/CT might lead to different results in the comparison. Another potential cause could be the different acquisition time of the transmission scan, 3mins versus 5mins in the present work.

Another study compared the AC TX to an atlas-based approach (Malone et al. 2011). Since the reference AC method was not the CT but the TX a relation to this work can only be partly derived. The authors could show that the reconstructed values of the TX and their atlas-based approach are in great accordance with r^2 greater than 0.97. However, on a close look at the atlas-based AC map the bone is depicted very thin indicating a probable underestimation if the approaches were compared to the CT. Therefore, their results are kind of in accordance with our findings that the AC TX underestimates the *SUVs* compared to the AC CT. It was elucidated that the underestimation might arise from statistical noise (Nakamoto et al. 2002).

Usually the AC TX is only applied to data originating from PET while the AC CT is used for the PET/CT and in research studies also for the PET/MR. In the present work the TX was applied to data which emerged from the PET/MR. The different *SUVs* of data reconstructed with AC CT and AC TX revealed the issue that the results of both scanners might not be comparable. Further it has to be hypothesized that one of the AC maps deliver wrong results. However, it might not be a problem if the studies are carried out on the same scanner so the error is the same for the whole scientific community. Nevertheless, for the opportunity to compare results between different scanners an evaluation where the differences arise from and a possibility to minimize them is needed.

A method which could probably enhance the performance of the AC TX approach would be segmenting the soft tissue by thresholding the values below bone. Since the error is higher in a greater distance to bone it is assumed that the LACs of the bone in AC TX are similar to the ones in AC CT. Alternatively, the LACs of the soft tissue are too small. By segmenting and applying a fixed value to soft tissue the uncertainties arising from the statistical noise should be reduced and the AC TX should perform better. However, this must be further evaluated. Furthermore, it might be enough to prolong the transmission scan to 10mins to improve the AC TX by reducing the noise.

Nonetheless, it was stated that the AC CT is more advantageous than the AC TX (Kinahan et al. 1998). The reason is that the AC CT has less statistical noise and therefore brings less noise to the reconstructed image. Furthermore, it can be recorded after the tracer injection. If the same is done for the TX the emitted 511keV photons would degrade the signal of the TX. In addition the CT can be performed much faster which is important to increase the comfort of

the patients and the scanner throughput which is relevant for the clinical routine. Lastly, since the rotating rod sources are decaying they have to be replaced which is a cost factor.

To sum up, it could be demonstrated that the AC TX might not be a good choice for substitution of the AC CT, neither for clinical route nor for research studies.

6. Conclusion

Correct AC of PET images obtained with hybrid PET/MR systems is still a challenging issue whereas numerous solutions have been proposed. MR images do not depict bone sufficiently for AC because of a small portion of hydrogen atoms. Therefore, alternative AC methods had to be invented. The most common AC for brain studies is the additional recording of a low-dose CT. However, this leads to the necessity of further processing steps, further radiation exposure for the subject and is not feasible for the clinical routine. Therefore, an easy to apply and accurate AC approach different to the CT is needed. The aim of the present work was to find such an alternative by comparing the performance of common strategies, namely an atlas-based approach, two segmentation based approaches and a transmission approach from rotating rod sources. The results revealed that the atlas-based approach performed best in terms of accuracy but as a drawback further processing is needed before it can be applied as AC map. The AC DIXON with tissue swap was not accurate but showed a high r^2 which opens the possibility of a linear scaling at least for the ROIs. A drawback is that the tissue swap occurs randomly and cannot be forced. The reported results of the RESOLUTE approach are also rather promising although the applicability for the clinical routine still has to be evaluated.

Conclusively, it can be said that a substitution of the AC CT is possible for research brain studies with AC pseudoCT and AC RESOLUTE. For the clinical routine the vendor would have to implement one of these techniques because of time-wise, personal and technical issues.

7. References

- Andersen, Flemming Littrup, Claes Nøhr Ladefoged, Thomas Beyer, Sune Høgild Keller, Adam Espe Hansen, Liselotte Højgaard, Andreas Kjær, Ian Law, and Søren Holm. 2014. "Combined PET/MR Imaging in Neurology: MR-Based Attenuation Correction Implies a Strong Spatial Bias When Ignoring Bone." *NeuroImage* 84: 206–16. doi:10.1016/j.neuroimage.2013.08.042.
- Bailey, Dale L. 1998. "Transmission Scanning in Emission Tomography." *European Journal of Nuclear Medicine* 25 (7): 774–87. doi:10.1007/s002590050282.
- Bailey, Dale L, David W Townsend, Peter E Valk, and Michael N Maisey. 2004. *Positron Emission Tomography: Basic Sciences*. Book. Springer Science & Business Media.
- Berker, Y., J. Franke, a. Salomon, M. Palmowski, H. C. W. Donker, Y. Temur, F. M. Mottaghy, et al. 2012. "MRI-Based Attenuation Correction for Hybrid PET/MRI Systems: A 4-Class Tissue Segmentation Technique Using a Combined Ultrashort-Echo-Time/Dixon MRI Sequence." *Journal of Nuclear Medicine* 53 (5): 796–804. doi:10.2967/jnumed.111.092577.
- Burgos, Ninon, M. Jorge Cardoso, Kris Thielemans, Marc Modat, Stefano Pedemonte, John Dickson, Anna Barnes, et al. 2014. "Attenuation Correction Synthesis for Hybrid PET-MR Scanners: Application to Brain Studies." *IEEE Transactions on Medical Imaging* 33 (12): 2332–41. doi:10.1109/TMI.2014.2340135.
- Carney, Jonathan P J, David W Townsend, Vitaliy Rappoport, and Bernard Bendriem. 2006. "Method for Transforming CT Images for Attenuation Correction in PET/CT Imaging." *Medical Physics* 33 (4): 976–83. doi:10.1118/1.2174132.
- Chung, June Key, Yu Kim, Seok Ki Kim, Yong Lee, Sunta Paek, Jeong Yeo, Jae Jeong, Dong Lee, Hee Jung, and Myung Lee. 2002. "Usefulness of 11C-Methionine PET in the Evaluation of Brain Lesions That Are Hypo- or Isometabolic on 18F-FDG PET." *European Journal of Nuclear Medicine* 29 (2): 176–82. doi:10.1007/s00259-001-0690-4.
- Delso, Gaspar, Sebastian Fürst, Björn Jakoby, Ralf Ladebeck, Carl Ganter, Stephan G. Nekolla, Markus Schwaiger, and Sibylle I. Ziegler. 2011. "Performance Measurements of the Siemens mMR Integrated Whole-Body PET/MR Scanner." *Journal of Nuclear Medicine* 52 (12): 1914–22. doi:10.2967/jnumed.111.092726.
- Delso, Gaspar, Axel Martinez-Moeller, Ralph A Bundschuh, Stephan G Nekolla, and Sibylle I Ziegler. 2010. "The Effect of Limited MR Field of View in MR/PET Attenuation Correction." *Medical Physics* 37 (6): 2804–12. doi:10.1118/1.3431576.
- Dickson, John C., Celia O'Meara, and Anna Barnes. 2014. "A Comparison of CT- and MR-Based Attenuation Correction in Neurological PET." *European Journal of Nuclear Medicine and Molecular Imaging* 41 (6): 1176–89. doi:10.1007/s00259-013-2652-z.
- Hahn, Andreas, Gregor Gryglewski, Lukas Nics, Marius Hienert, Lucas Rischka, Chrysoula Vraka, Helen Sigurdardottir, et al. 2016. "Quantification of Task-Specific Glucose Metabolism with Constant Infusion of 18F-FDG." *Journal of Nuclear Medicine*. doi:10.2967/jnumed.116.176156.

- Huang, S C, E J Hoffman, M E Phelps, and D E Kuhl. 1979. "Quantitation in Positron Emission Computed Tomography: 2. Effects of Inaccurate Attenuation Correction." *Journal of Computer Assisted Tomography* 3 (6): 804–14.
- Ishii, Kazunari, Frode Willoch, Satoshi Minoshima, Alexander Drzezga, Edward P Ficaró, Donna J Cross, David E Kuhl, and Markus Schwaiger. 2001. "Statistical Brain Mapping of 18F-FDG PET in Alzheimer's Disease: Validation of Anatomic Standardization for Atrophied Brains." *The Journal of Nuclear Medicine* 42 (4): 548–57. <http://jnm.snmjournals.org/cgi/content/abstract/42/4/548>.
- Keereman, Vincent, Yves Fierens, Tom Broux, Yves De Deene, Max Lonneux, and Stefaan Vandenberghe. 2010. "MRI-Based Attenuation Correction for PET/MRI Using Ultrashort Echo Time Sequences." *Journal of Nuclear Medicine: Official Publication, Society of Nuclear Medicine* 51 (5): 812–18. doi:10.2967/jnumed.109.065425.
- Keller, Sune H., Søren Holm, Adam E. Hansen, Bernhard Sattler, Flemming Andersen, Thomas L. Klausen, Liselotte Højgaard, Andreas Kjær, and Thomas Beyer. 2013. "Image Artifacts from MR-Based Attenuation Correction in Clinical, Whole-Body PET/MRI." *Magnetic Resonance Materials in Physics, Biology and Medicine* 26 (1): 173–81. doi:10.1007/s10334-012-0345-4.
- Kinahan, P E, D W Townsend, T Beyer, and D Sashin. 1998. "Attenuation Correction for a Combined 3D PET/CT Scanner." *Medical Physics* 25 (10): 2046–53. doi:10.1118/1.598392.
- Koesters, Thomas, Kent Parks Friedman, Matthias Fenchel, Yiqiang Zhan, Gerardo Hermosillo, James Babb, Ileana O Jelescu, David Faul, Fernando E Boada, and Timothy M Shepherd. 2016. "Dixon Sequence with Superimposed Model-Based Bone Compartment Provides Highly Accurate PET/MR Attenuation Correction of the Brain." *Journal of Nuclear Medicine: Official Publication, Society of Nuclear Medicine*, jnumed.115.166967-. doi:10.2967/jnumed.115.166967.
- Ladefoged, Claes N, Didier Benoit, Ian Law, Soren Holm, Andreas Kjaer, Liselotte Højgaard, Adam E Hansen, and Flemming L Andersen. 2015. "Region Specific Optimization of Continuous Linear Attenuation Coefficients Based on UTE (RESOLUTE): Application to PET/MR Brain Imaging." *Physics in Medicine and Biology* 60 (20): 8047–65. doi:10.1088/0031-9155/60/20/8047.
- Ladefoged, Claes Nøhr, Adam Espe Hansen, Sune Høgild Keller, Søren Holm, Ian Law, Thomas Beyer, Liselotte Højgaard, Andreas Kjær, and Flemming Littrup Andersen. 2014. "Impact of Incorrect Tissue Classification in Dixon-Based MR-AC: Fat-Water Tissue Inversion." *EJNMMI Physics* 1 (1): 101. doi:10.1186/s40658-014-0101-0.
- Lee, Dong Soo, Hyejin Kang, Heejung Kim, Hyojin Park, Jungsu S. Oh, Jae Sung Lee, and Myung Chul Lee. 2008. "Metabolic Connectivity by Interregional Correlation Analysis Using Statistical Parametric Mapping (SPM) and FDG Brain PET; Methodological Development and Patterns of Metabolic Connectivity in Adults." *European Journal of Nuclear Medicine and Molecular Imaging* 35 (9): 1681–91. doi:10.1007/s00259-008-0808-z.
- Malone, Ian B, Richard E Ansorge, Guy B Williams, Peter J Nestor, T Adrian Carpenter, and Tim D Fryer. 2011. "Attenuation Correction Methods Suitable for Brain Imaging with a PET/MRI Scanner: A Comparison of Tissue Atlas and Template Attenuation Map

- Approaches." *Journal of Nuclear Medicine : Official Publication, Society of Nuclear Medicine* 52 (7): 1142–49. doi:10.2967/jnumed.110.085076.
- Martinez-Möller, Axel, Michael Souvatzoglou, Gaspar Delso, Ralph a Bundschuh, Christophe Ched'hotel, Sibylle I Ziegler, Nassir Navab, Markus Schwaiger, and Stephan G Nekolla. 2009. "Tissue Classification as a Potential Approach for Attenuation Correction in Whole-Body PET/MRI: Evaluation with PET/CT Data." *Journal of Nuclear Medicine : Official Publication, Society of Nuclear Medicine* 50 (4): 520–26. doi:10.2967/jnumed.108.054726.
- Mosconi, Lisa, Rachel Mistur, Remigiusz Switalski, Wai Hon Tsui, Lidia Glodzik, Yi Li, Elizabeth Pirraglia, et al. 2009. "FDG-PET Changes in Brain Glucose Metabolism from Normal Cognition to Pathologically Verified Alzheimer's Disease." *European Journal of Nuclear Medicine and Molecular Imaging* 36 (5): 811–22. doi:10.1007/s00259-008-1039-z.
- Nakamoto, Yuji, Medhat Osman, Christian Cohade, Laura T Marshall, Jonathan M Links, Steve Kohlmyer, and Richard L Wahl. 2002. "PET/CT: Comparison of Quantitative Tracer Uptake between Germanium and CT Transmission Attenuation-Corrected Images." *Journal of Nuclear Medicine : Official Publication, Society of Nuclear Medicine* 43 (9): 1137–43. <http://www.ncbi.nlm.nih.gov/pubmed/12215550>.
- Paulus, Daniel H, Harald H Quick, Christian Geppert, Matthias Fenchel, Yiqiang Zhan, Gerardo Hermosillo, David Faul, Fernando Boada, Kent P Friedman, and Thomas Koesters. 2015. "Whole-Body PET/MR Imaging: Quantitative Evaluation of a Novel Model-Based MR Attenuation Correction Method Including Bone." *Journal of Nuclear Medicine : Official Publication, Society of Nuclear Medicine* 56 (7): 1061–66. doi:10.2967/jnumed.115.156000.
- Phelps, Michael E., Simon R. Cherry, and Magnus Dahlbom. 2006. *PET: Physics, Instrumentation, and Scanners. PET: Physics, Instrumentation, and Scanners*. doi:10.1007/0-387-34946-4.
- Pichler, Bernd J., Hans F. Wehrl, Armin Kolb, and Martin S. Judenhofer. 2008. "Positron Emission Tomography/Magnetic Resonance Imaging: The Next Generation of Multimodality Imaging?" *Seminars in Nuclear Medicine*. doi:10.1053/j.semnuclmed.2008.02.001.
- Pike, Victor W. 2009. "PET Radiotracers: Crossing the Blood-Brain Barrier and Surviving Metabolism." *Trends in Pharmacological Sciences*. doi:10.1016/j.tips.2009.05.005.
- Saha, Gopal B. 2005. *Basics of PET Imaging. Imaging*. Vol. 202. doi:10.1007/978-1-4419-0805-6.
- Samarin, Andrei, Cyrill Burger, Scott D. Wollenweber, David W. Crook, Irene A. Burger, Daniel T. Schmid, Gustav K. Von Schulthess, and Felix P. Kuhn. 2012. "PET/MR Imaging of Bone Lesions - Implications for PET Quantification from Imperfect Attenuation Correction." *European Journal of Nuclear Medicine and Molecular Imaging* 39 (7): 1154–60. doi:10.1007/s00259-012-2113-0.
- Stoecker, Tony, and Nadim Jon Shah. 2007. "Funktionelle MRT in Psychiatrie Und Neurologie." In *Funktionelle MRT in Psychiatrie Und Neurologie*, 359–74. doi:10.1007/978-3-540-68558-6.

Tzourio-Mazoyer, N, B Landeau, D Papathanassiou, F Crivello, O Etard, N Delcroix, B Mazoyer, and M Joliot. 2002. "Automated Anatomical Labeling of Activations in SPM Using a Macroscopic Anatomical Parcellation of the MNI MRI Single-Subject Brain." *NeuroImage* 15 (1): 273–89. doi:10.1006/nimg.2001.0978.

Table of figures

Figure 1: Annihilation event with the paths of the resulting photons. The dotted line describes the detected LOR. The illustration was taken from Bailey et al. (2004).....	11
Figure 2: For a quantitatively correct reconstructed image the data has to be corrected for randoms, scatter, dead time and attenuation. The attenuation correction is carried out with a blank and transmission scan with an external radioactive source. Factors from detector normalization have to be applied due to the difference performance of the PMTs. The emission and attenuation correction data are represented as sinograms. The image was taken from Bailey et al. (2004).....	15
Figure 3: The conventional detectors in PET are PMTs (left) whereas APDs are used in PET/MR (right). The lower images show detector element maps. On the left it can be seen that the PMT detectors are sensitive to a magnetic field. A small horse magnet was placed near the detector. Differently, the APD-based detector map is not affected by a magnetic field, not even for 7T. Image taken from Pichler et al. (2008).....	18
Figure 4: Simplified flow chart of the processing steps from the original CT to the final AC CT	24
Figure 5: Structural T1-weighted target MRI uploaded to the provided website of the University College London	25
Figure 6: Returned pseudoCT which results from the provided target MRI (see Figure 5), optimized for accuracy	26
Figure 7: Fat image calculated from the in- and opposed-phase images, produced by the Siemens Biograph mMR scanner	26
Figure 8: Water image calculated from the in- and opposed-phase images, produced by the Siemens Biograph mMR scanner	27
Figure 9: (A) correct DIXON (B) DIXON with fat, water tissue swap (C) correct DIXON with cancelled signal in the area of the mouth, due to a retainer. Soft tissue, fat and air are depicted in white, gray and black, respectively.	27
Figure 10: Result of the segmentation of the R2 map as obtained from the scanner with bone in white, soft tissue in gray and air in black	28

Figure 11: Transmission scan transformed to AC map with AC DIXON attached to area without information. Bone is clearly visible in white, soft tissue in gray. It can be seen, that the center of the head has similar LACs compared to the neck region of the AC DIXON, namely soft tissue..... 29

Figure 12: Hardware AC map of the bed and head coil 30

Figure 13: ROI-based correlation between *SUVs* of the reconstruction with AC CT and AC pseudoCT (left). The scatter plot shows high correlation ($r^2 = 0.99$), a slope of almost 1 and an intercept near 0, indicating a similarity of the *SUVs* and also of the AC maps to a great extent. The Bland-Altman plot (right) shows a small fluctuation margin around the center at -0.02 revealing a slight underestimation for the values reconstructed with AC pseudoCT. Therefore, the similar performance of both AC approaches is also supported by the Bland-Altman plot. 34

Figure 14: Voxel-wise difference map in percent between *SUVs* reconstructed with AC CT and AC pseudoCT. The difference map shows small differences up to 4% in occipital regions and a difference of around 10-15% in frontal and lateral regions close to bone tissue. Errors above 30% are outside of the brain and can be ignored for this work. 35

Figure 15: Statistical result of the paired t-test with $T > 8.59$, $p < 0.05$ FWE corrected, as threshold. The difference between *SUVs* reconstructed with AC CT and *SUVs* reconstructed with AC pseudoCT is significant only for two small lateral regions and outside of the brain. 35

Figure 16: Correlation of ROIs between *SUVs* reconstructed with AC CT and AC DIXON_{all} (left). The scatter plot shows low correlation ($r^2 = 0.71$), a slope of 0.84 and an intercept close to zero. This indicates an underestimation of the reconstructed values with AC Dixon. The Bland-Altman plot (right) reveals a great deviation and underestimation from the center at -0.3, especially for higher binding regions. Furthermore, the patterns of the plotted data lead to the suggestion that the dataset should be split based on a feature for better correlation. 36

Figure 17: Voxel-wise difference map in percent of *SUVs* reconstructed with AC CT and AC DIXON_{all}. The difference map shows an increasing error from the center of the brain (approximately 10%) to the regions close to bone tissue (approximately 30%). It should be remarked, brain regions can be distinguished by means of difference such as the thalamus. Although the difference map displays differences up to 50% these are in the border to the skull..... 37

Figure 18: Statistical result of the paired t-test with $T > 8.47$, $p < 0.05$ FWE corrected, as threshold. The difference of *SUVs* reconstructed with AC CT and *SUVs* reconstructed with AC DIXON_{all} shows significant errors in the proximity of bone and therefore significant underestimations in this region.. 37

Figure 19: Correlation of ROIs between reconstruction AC CT and AC Dixon_{ok} (left). The scatter plot shows medium to high correlation ($r^2 = 0.87$). The regression line with a slope below 1 and an intercept

close but below zero indicates continuous underestimations of the *SUVs*. The Bland-Altman plot shows a great deviation around the center of -0.22 and therefore an underestimation of the reconstructed values. 38

Figure 20: Voxel-wise difference map in percent of *SUVs* reconstructed with AC CT and AC DIXON_{ok}. The difference map shows an increasing error from the center of the brain (approximately 4%) to the regions close to bone tissue (approximately 20%). It should be remarked, brain regions can be distinguished by means of their difference such as the thalamus. 38

Figure 21: Statistical result of the paired t-test with $T > 11.57$, $p < 0.05$ FWE corrected, as threshold. The difference off reconstruction with AC CT and reconstruction AC Dixon_{all} shows significant errors across the whole brain except for small frontal regions. 39

Figure 22: Correlation of ROIs between *SUVs* reconstructed with AC CT and AC Dixon_{ok} (left). The scatter plot shows higher correlation than the reconstructions with AC Dixon_{all} and AC Dixon_{ok}. Although the regression line indicates a great underestimation it should be possible to correct for the miscalculations with linear scaling due to the high correlation. The Bland-Altman plot (right) shows a large variation around the center of -0.51. The center far below 0 also demonstrates underestimation which increases with higher binding regions. Furthermore, the pattern found in the Bland-Altman plot indicates that ROIs with a lower uptake are less underestimated than regions with a high uptake. 39

Figure 23: Voxel-wise difference image in percent for *SUVs* reconstructed with AC CT and AC DIXON_{ts}. The difference map shows a higher error for the center of the brain (approximately 30%) than near bone (approximately 20%) and a higher error across the whole brain compared to DIXON_{all} and DIXON_{ok}. 40

Figure 24: Correlation of ROIs between *SUVs* reconstructed with AC CT and AC DIXON_{all}. It is the same figure as Figure 16 except for the colors, data of DIXON_{ok} in blue and data of DIXON_{ts} in red. The plots explain the different patterns and reveal that it is necessary to separate the analysis of DIXON_{ok} and DIXON_{ts} due to different performances. 40

Figure 25: Voxel-wise difference map in percent for reconstruction with AC CT and AC UTE. The difference map shows a smaller error for the center of the brain (approximately 5%) than near bone (approximately 15%). A smaller overall error is in correspondence with the scatter and Bland-Altman plot. It should be remarked, brain regions can be distinguished by means of their difference such as the putamen. 41

Figure 26: Correlation of ROIs between *SUVs* reconstructed with AC CT and AC UTE (left). The scatter plot shows high correlation and a regression line (slope = 0.93, intercept = -0.02) which

indicates small underestimations. The Bland-Altman plot on the right shows medium variation around the center of -0.14 which means small underestimation should be expected. 41

Figure 27: Statistical result of the paired the t-test with $T > 8.55$, $p < 0.05$ FWE corrected, as threshold. The difference of reconstruction with AC CT and reconstruction with AC pseudoCT shows significant errors across the whole brain except for caudal and frontal regions and the cerebellum. 42

Figure 28: Correlation of ROIs between *SUVs* reconstructed with AC CT and AC TX_{all} (left). The scatter plot shows medium correlation and a regression line with slope = 0.92 and intercept = -0.03 showing moderate underestimations. The Bland-Altman plot on the right shows a similar variation around the center at -0.14 as AC UTE which confirms that underestimation should be expected..... 42

Figure 29: Voxel-wise difference map in percent for reconstruction with AC CT and AC TX_{all}. The difference map shows a smaller error at the proximity to bone tissue (approximately 5%) and a higher error close to the center of the brain (approximately 25%) which is the opposite to what was already shown for DIXON and UTE. 43

Figure 30: Statistical result of the paired t-test with $T > 9.53$, $p < 0.05$ FWE corrected, as threshold. The difference between AC CT and AC TX_{all} was significant across the whole brain except for regions close to the bone. 43

Figure 31: Correlation of ROIs between *SUVs* reconstructed with AC CT and AC TX_{ok} (left). The scatter plot shows medium correlation ($r^2 = 0.83$) and a regression line with slope of 0.89 and of intercept = 0.02 leading to moderate underestimations. The Bland-Altman plot on the right shows variation of 12% around the center at -0.19. Both results are similar to the ones shown for TX_{all}. 44

Figure 32: Voxel-wise difference map in percent for reconstruction with AC CT and AC TX_{ok}. The resulting difference map shows almost the exact same error as for TX_{all}: The error near bone tissue is around 5% and near the center 25%. 44

Figure 33: Statistical result of the paired t-test with $T > 14.32$, $p < 0.05$ FWE corrected, as threshold. The difference of reconstruction with AC CT and reconstruction with AC TX_{ok} shows significant errors comparable to TX_{all} but thinned out, probably due to the smaller sample size..... 45

Figure 34: Correlation of ROIs between *SUVs* reconstructed with AC CT and AC TX_{ts} (left). The scatter plot shows high correlation ($r^2 = 0.92$) and a regression line with a slope of 0.94 and an intercept of -0.09 which is in the range of TX_{ok} and TX_{all}. Also the Bland-Altman plot (left) is in the same scale as TX_{ok} and TX_{all} in terms of variation and the center at -0.2. 45

Figure 35: Voxel-wise difference map in percent for reconstruction with AC CT and AC TX_{ts}. The resulting difference map shows almost the exact same error as for TX_{all} and TX_{ok} : The error near bone tissue is around 5% and in this case an error near the center of the brain of around 30%..... 46

Figure 36: Correlation of ROIs between SUVs reconstructed with AC CT and AC TX_{all}. It is the same figure as Figure 28 except for the colors, data of TX_{ok} in blue and data of TX_{ts} in red. The plots do not show different patterns such as DIXON_{all} leading to the assumption that the LACs of the neck region do not influence the AC in the brain. 46

Figure 37: Summary of all presented AC maps: (A) CT, (B) pseudoCT, (C) correct DIXON, (D) DIXON tissue swap, (E) UTE, (F) Transmission with DIXON in neck region. 47